# POLITECNICO DI TORINO

Corso di Laurea Magistrale
in Ingegneria Energetica e Nucleare

Tesi di Laurea Magistrale

**Innovative numerical methods to investigate flow in screw compressors**

**Relatore:**
Andrea Ferrero

**Relatore:**
Francesco Larocca

**Candidato:**
Emanuele Antonio Napoli

# Summary

The purpose of this work is the study of the behavior of the internal flow in screw compressors. Screw compressor performances are affected mostly by the tooth profile which is fully defined in Section 5. In particular, parameters as sealing line and blow hole area must be minimized. Unfortunately profile curves and geometrical parameters, such as undercutting limits, are usually not available in the literature due to the need of manufacturing companies to protect their know-how and so it is difficult to find validation test cases. Since screw compressor are very complex machines which involves either moving and fixed parts, the CFD study of their behavior is difficult because it is necessary to generate a suitable time-dependent grid which fully describes the change in shape of the control volume. This problem is overcome with the innovative strategy presented on this work. It is based on a penalization method, which is discussed in Section 2, integrated in a Discontinuous Galerkin spatial discretization described in Section 3.

The proposed approach is applied on various standard test cases in order to evaluate its reliability and accuracy, deeply argued in Section 6. After that the flow in 2D roots and screw compressors are investigated respectively in Section 7 and 8. The goal is to compare results obtained from simulation, such as flow rate and power, with the data available in the literature. In particular, the mass flow is compared with results available in literature showing good qualitative agreement. However, the difficulty to find both geometrical and experimental data in the literature for 2D configurations makes it impossible to perform a direct validation. Conclusions and further developments are reported in Section 9.

# Acknowledgments

I would like to thank my supervisors, Andrea Ferrero for all the time he dedicated to my doubts and questions and Francesco Larocca for his precious advise.
I would like to thank HPC@Polito for the computational resources that were used for the simulations presented in this work.
I am very grateful to my family for the support and to all my friends who never give up on me.

# Index

## Table of Figures

# Index of Tables

# Chapter 1 - Introduction

A volumetric compressor is a mechanical device which aims to increase the pressure of the working fluid by reducing its volume. It is contained into a casing, which together form a working chamber whose volume depends only on the angle of rotation. Depending on the flow direction, it may be used either for expansion or compression. They can be divided in two class of compressor: positive displacement and dynamic. The focus of this work will be on the first type, in particular on screw compressors. In fact they have many advantages over other positive displacement types. Firstly, all moving parts rotate and hence can reach much higher velocity, in opposition of reciprocating machines. Secondly, the contact forces within them are low, which make screw compressor more reliable than vane machines. Thirdly, and less know, unlike the reciprocating, scroll and vane machines, all sealing lines of contact which define the limit of the compressing chamber, decrease in length as the size of the working chamber decreases and the pressure within rises, this minimizes leakages from chamber during the compression process [1]. Screw compressors are composed by two matched rotating positive-displacement helical-screws which compress reducing the space in which air is trapped. This type of machines are characterized by high reliability, ease of operation, low vibration, high adaptability and the ability to transport various mixture of fluids. They are widely used in many continuous commercial and industrial applications such as food processing, medicine manufacturing, air conditioning and refrigeration. Their pressure outlet can reach 8 Mpa and the typical absorbed power is between 2.2 kW to over 890 kW. Each type of application has particular constraints such as efficiency, size, cost, purity of the gas treated or flow rate. For instance in refrigeration processes, compressors operate for long period and must have higher efficiency as possible, or, in case of air compressor, in particular for mobility applications, efficiency may be less important than size and cost.

Three types of screw compressor are commercially produced: Oil Flooded, Water flooded and Dry type. As the names suggest, the oil flooded compressor is cooled down with oil as refrigerant and the water flooded one is cooled down with water. If a particular valuable gas is treated, a dry type, without refrigerant, may be required in order to have not contaminants. They all have both advantages and disadvantages. The dry screw compressor can not exploit the injection of oil or water to reduce the leak of compressed air. In order to overcome this issue, the rotor velocity must increase. This led to higher noise value and, since there is not a coolant, the discharge temperature reaches 300°C or higher. Oil flooded type compressor are characterized by lower speed of rotation since the rotor gaps can be sealed by oil. Furthermore, the provided compressed gas has lower temperature since it is cooled by oil. Unfortunately, the use of oil makes hard and costly to maintain and requires environmental measures. The water-flooded oil-free screw compressor, injecting water as refrigerant, removes disadvantages of both oil-flooded and dry type screw compressor since a coolant is present in order to reduce temperature at the outlet and the fluid is not contaminated. In fact water in the outlet stream can be collected by a condenser [2].

Since this type of machine is widely used, there is an increasing demand for performance improvements such as flow rates, operating pressures, reducing pollution and increasing efficiency. These issues are solved improving tools provided by the computational fluid dynamics (CFD). Nowadays CFD is used in most of engineering and scientific areas in order to predict physical quantities involved in a specific process. CFD simulations are based on the numerical solution of the conservation law of mass, momentum and energy for a determined case study. The standard way to numerically solve governing equations is the use of the Finite Volume Method (FVM).

Internal unsteady flows in screw compressor were considered of secondary importance for long time, but the increasing demand for more accurate prediction flows in various types of devices led to spend many efforts in order to improve and overcome many mathematical problems. This work was done especially for internal flows within moving boundaries basically because the ability to predict quite accurately flows in screw compressor can give many advantages to manufacturers. FVM has been used to solve these types of problems, as demonstrated by Peric (1985), Demirdzic and Peric (1990) and Demirdzic and Muzaferijia (1995). Unfortunately, as far as FVM is applied to internal flows with moving domain, there are two basic issues which make their resolution really difficult. First, the flow inside a screw machine can vary remarkably because of the complex geometry. Second, it may be a problem substituting such domain with a computational grid of good quality which allows sufficiently accurate and reliable calculation.

The first approaches which describe screw compressors by CFD methods did not give good results because of the inability to generate a suitable enough grid for complex geometries. The deadlock was over when analytical transfinite interpolation with adaptive mesh was used to automatically map an arbitrary screw machine [3]. Basically an algebraic approach can be used to calculate the interior points of the grid through transfinite interpolation, which is a multivariate interpolation procedure. The approach is simple and it can be able to generate quickly a grid. However, if the region has a complex shape, generated cells can be very narrow so that cells can overlap or overcome the boundary limits. Algebraic methods are able to generate a screw compressor mesh of a desired quality, if it is used in conjunction with boundary adaptation and procedure to obtain orthogonal grids [4].

Analytical transfinite interpolation is completely explained by Kovacevic in [3]. The presented method was then implemented in a grid generation program called SCORG- Screw Complessor Rotor Geometry Grid generator. This software provides a mesh for both moving and stationary part of the machine and performs direct integration in commercial CFD codes. Unfortunately SCORG is a software which is not of public domain.

In this work the use of a method capable of solving the CFD equations without particularly constraints on the used grid will be investigated. This method, at least ideally, is able to solve CFD problems which involve complex-moving geometry without particular requirement on the used mesh. It is Discontinuous Galerkin Method with penalization terms to reproduce the effect of the body.

# Chapter 2 - Physical model

As far as CFD simulation are concerned, widely adopted grids are mainly of two types: body-fitted grids and embedded grids. The first one, as the name suggests, fits perfectly with the boundaries of the body and the external borders of the domain. This means that, most of the time, following the boundaries led to the creation of deformed elements characterized by poor value of skewness angle, smoothness and aspect ratio. The second approach consists on the creation of grids which match up only the external boundaies of computational domain and which includes bodies, so they are not described directly by the mesh. Particular attention must be given to elements near the boundaries of the body. In this way, the bodies result immersed inside a large mesh. However, the main issue of this type of grid is the proper setting of the boundary conditions and the boundaries themselves. The adoption of embedded grids is also known as immersed boundary method (IBM) [5].

In this work IBM is adopted because it simplifies the issues related to the mesh, particularly when dealing with moving bodies and changing of control volumes, and because it makes wall boundary treatment easier when penalization method is used to enforce the boundary conditions.

The choice of the physical model which describes properly the real phenomena under investigation is the main concern in a CFD simulation. Specifically, the adopted method should be a trade of between computational cost and accuracy in terms of reproducing the physical of studied phenomena.

In the following the physical model adopted, the space and time discretization will be treated.

# 2.1 - Navier-Stokes equations

The model chosen to describe the flow inside screw compressors is described by the compressible Navier-Stokes equations. As reported in [6], the adimensionalized equations can be written as follows:

$$\frac{\partial \rho}{\partial t}+\frac{\partial}{\partial x_j}(\rho u_j)=0 \tag{2.1}$$

$$\frac{\partial}{\partial t}(\rho u_i)+\frac{\partial}{\partial x_j}(\rho u_i u_j)=-\frac{\partial P}{\partial x_i}+\frac{1}{Re_{ref}}\frac{\partial \tau_{ij}}{\partial x_j} \tag{2.2}$$

$$\frac{\partial E}{\partial t}+\frac{\partial}{\partial x_j}(u_j(E+P))=\frac{1}{(Re_{ref})}\frac{\partial}{\partial x_j}[u_i \tau_{ij}-q_i] \tag{2.3}$$

The heat flux $q_i$ is described by the Fousier law: $q_i=-\frac{\gamma}{(\gamma-1)}\frac{\mu}{Pr}\frac{\partial T}{\partial x_i}$ .

The heat conductivity $\lambda$ is expressed in terms of dynamic viscosity $\mu$ and the Prandtl number $Pr$ . Both heat conductivity $\lambda$ and dynamic viscosity $\mu$ are assumed constant. If necessary, the Sutherland's law, which describes the variation of dynamic viscosity with temperature, can be easily activated. As far as the shear-stress tensor $\tau_{ij}$ is concerned, the Boussinesq approach is used and, assuming the Stoke's hypothesis for bulk viscosity, it results in

$$\tau_{ij}=2\mu\left[S_{ij}-\frac{1}{3}\frac{\partial u_k}{\partial x_k}\delta_{ij}\right]$$

where $S_{ij}$ is the mean strain rate tensor:

$$S_{ij}=\frac{1}{2}\left(\frac{\partial u_i}{\partial x_j}+\frac{\partial u_j}{\partial x_i}\right)$$

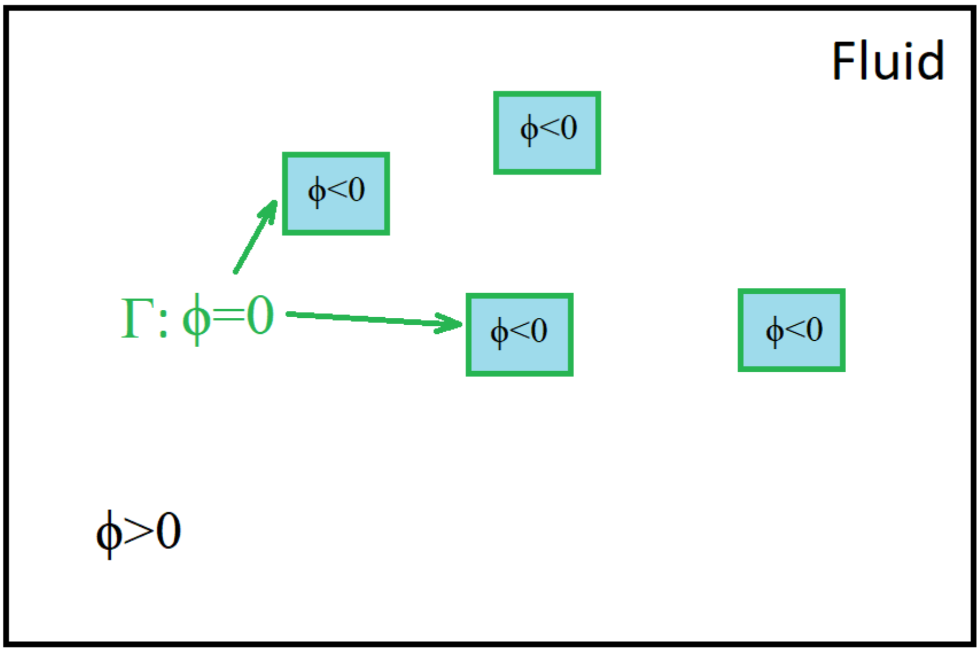


*Figure 1: Schematic representation of the computational domain* $\Omega=\Omega_f\cup\Omega_S$ *. $S_i$ represents a solid domain and* $\Gamma=\partial\Omega$ *represents the solid boundary.*

In order to enhance the no-slip boundary condition inside the solid bodies, a penalization method [5] was adopted. The basic idea beside the penalization method, or Brinkman-Navier-Stokes equations, is to consider solids as porous media with a really small permeability. A level set function $\Phi$ identifies boundaries and allow to describe the motion of solid bodies [7]. More in detail, imagine a computational domain $\Omega$ in which solid bodies $S^i$ are immersed. The compressible flow is situated around bodies in $\Omega_f$ as shown Fig. 1.

Given the condition of:

$\boldsymbol{u}=\boldsymbol{u}_{S^i}$ on $\partial S^i$

$\boldsymbol{u}=\boldsymbol{u}_f$ on $\partial\Omega_f$

the problem of fluid-solid interaction can be described by compressible N-S equations together with the proper Dirichlet and Neuman conditions on temperature. The velocity assumes two different values according to the position of computational domain considered: $\boldsymbol{u}_f$ in the fluid and $\boldsymbol{u}_{S^i}$ in the solid bodies. In order to satisfied the no-slip condition this two values must be equal on Γ. A penalization term is used to extend the velocity field inside the solid bodies in order to impose a rigid motion inside the solid. Setting $\frac{1}{\eta} \gg 1$ where $\eta$ is the penalization parameter, and calling $\chi_{S_i}$ the characteristic function of the solid $S_i$, the compressible N-S equation with penalization has the following form:

$$\frac{\partial \rho}{\partial t} + \frac{\partial}{\partial x_j}(\rho u_j) = 0 \tag{2.4}$$

$$\frac{\partial}{\partial t}(\rho u_i) + \frac{\partial}{\partial x_j}(\rho u_i u_j) = -\frac{\partial P}{\partial x_i} + \frac{1}{Re_{ref}} \frac{\partial \tau_{ij}}{\partial x_j} + \frac{1}{\eta} \sum_{i=1}^{N_s} \chi_{S^i}(\rho u_i - \rho u_{i,S^i}) \tag{2.5}$$

$$\begin{aligned} \frac{\partial E}{\partial t} + \frac{\partial}{\partial x_j}(u_j(E+P)) = \frac{1}{(Re_{ref})} \frac{\partial}{\partial x_j}[u_i \tau_{ij} - q_i] + \frac{1}{\eta} \sum_{i=1}^{N_s} \theta_{S^i} \chi_{S^i} \rho \left| \epsilon(T) - \epsilon(T_{S_i}) \right| + \\ + \frac{1}{\eta} \sum_{i=1}^{N_s} \chi_{S^i} \rho \left| \rho u_i - \rho u_{i,S^i} \right| u_j \end{aligned} \tag{2.6}$$

with $\varepsilon(T)=c_v T$ . Remember that $\eta$ is considered as an adimensionalized time.

The derivation of this system of equation is reported in [5]. Since the penalization factor is a very large number, the difference between the required temperature and the fluid temperature at the wall is the main contribution of the energy equation near the solid boundary. In this way, if $\theta_{S^i}=1$ is set, the Dirichlet condition on temperature can be easily imposed. Instead, if $\theta_{S^i}=0$ is set, homogeneous Neumann boundary condition on temperature (adiabatic condition) can be imposed.

The way in which the previous system of equations is discretized and integrated affect the choice of the penalization factor value (*1/η*). In fact, ideally it must be the larger as possible in order to have a better results given by penalization method, but effectively is related to the mesh size and the integration method.

The factor $\chi_{S^i}$ is defined starting from the level set function $\Phi_{S^i}$ . The level set is initialized as the distance with sign between a generic point of the grid and the nearest point of the solid boundary. In this way $\Phi_{S^i}$ results positive outside the solid and negative inside $S_i$. The factor $\chi_{S^i}$ is defined as:

$$\chi_{S^i}=\begin{cases}1 & if \;\; \Phi_{S^i}\leq 0\\ 0 & if \;\; \Phi_{S^i}>0\end{cases} \tag{2.7}$$

If the body is moving, $\Phi_{S^i}$ has to satisfy the following equation:

$$\frac{\partial \Phi_{S^i}}{\partial t}+(u_{i,S^i}\frac{\partial \Phi_{S^i}}{\partial x_i})=0 \qquad for\, x_i\in\Omega_f \tag{2.8}$$

which represents the transport of the level set function.

In this case, since $u_{i,S^i}$ is a rigid motion, the level set function $\Phi_{S^i}$ remains always a signed distance.

# Chapter 3 - Discontinuous Galerkin spatial discretization

The discontinuous Galerkin method (DGM) merges the main advantageous characteristics of both finite elements (FEM) and finite volume (FVM) methods. In particular, it is based on numerical fluxes which use piecewise polynomial (from FEM) but discontinuous (from FVM) approximations which allow to reach high order of accuracy. It can also deal with discontinuities in solutions or steep gradients such as in solutions of convection-diffusion equations dominated by convection. However, the method used in DGM to obtain high-order accuracy in space discretization is different from FV methods. Indeed, in FV methods the mean value of the conservative variables in the cell is available for the reconstruction. So, in order to reach high-order reconstruction, many neighbouring cells must be used when working with FVM. Instead in DGM many degrees of freedom (DOFs) are introduced in the cell. This method simplifies the reconstruction because all needed information is already contained in the cell.

This method can also easily handle unstructured grids, which give an advantage in this work in which complex geometries are studied.

For more information on DGM see, [8] and [6].

## 3.1 - Variational approach

The physical model considered with DG space discretization in 2D for the vector $U$ of conservative variables can be written as follow:

$$\frac{\partial \boldsymbol{U}}{\partial t}+\frac{\partial \boldsymbol{F}}{\partial x}+\frac{\partial \boldsymbol{G}}{\partial y}=\boldsymbol{Q} \qquad (x,y)^T \in \Omega \subset R^2, t \in R_0^{+} \tag{3.1}$$

where $\boldsymbol{U}$ is the conservative variable vector, **F** and **G** contain the advection and the viscous fluxes and **Q** is a generic source term. In this case **Q** is the vector which contains the penalization terms:

$$\boldsymbol{Q}=\frac{1}{\eta}\sum_{i=1}^{N_S} \chi_{S^i} \begin{pmatrix} 0 \\ \rho \boldsymbol{u}-\rho \boldsymbol{u}_{S^i} \\ \frac{S_{ref} T_{ref}}{\boldsymbol{u}_{ref}^2} \theta_{S^i} \rho(\epsilon(T)-\epsilon(T_{S^i}))+\rho(\boldsymbol{u}-\boldsymbol{u}_{S^i})\cdot \boldsymbol{u} \end{pmatrix} \tag{3.2}$$

Assuming that $\Omega$ is subdivided in a set of non-overlapping cells $\Omega_e$, consider a generic element $\Omega_e$. Consider also the functional space $V_h$ defined as

$$V_h=\{v \in L^2(\Omega): v|_{\Omega_e} \in P^p(\Omega_e) \quad \forall \Omega_e \in T_h\} \quad .$$

$V_h$ approximates the solution in $\Omega_e$ with a space polinomial $P^p(\Omega_e)$ of degree up to $p$. The main feature is that no continuity constraints are required across the element edges in the space $V_h$ and the order $p$ of reconstruction can vary in each element. Defining $\Psi_i$ the basic functions of $V_h$, the numerical solution $u_h$, which belongs to $V_h$ , can be written as a linear combination of the basic functions:

$$u_h(\boldsymbol{x},t)=\tilde{\boldsymbol{u}}\cdot\boldsymbol{\Psi}=\sum_{i=1}^{N_e}\tilde{u}_i\Psi_i \tag{3.3}$$

Equation 3.3 is then substituted in 2.4, 2.5, 2.6 to obtain the residual $R_h$ defined as:

$$R_h=\frac{\partial u_h}{\partial t}+\frac{\partial \boldsymbol{F}_h}{\partial x}+\frac{\partial \boldsymbol{G}_h}{\partial y}-\boldsymbol{Q} \quad .$$

The DGM requires that the projection on the $V_h$ space of the residual integral on $\Omega_e$ is null:

$$\int_{\Omega_e} R_h\, v dxdy=\int_{\Omega_e}\frac{\partial u_h}{\partial t}\, vdxdy+\int_{\Omega_e}\frac{\partial \boldsymbol{F}_h}{\partial x}\, vdxdy+\int_{\Omega_e}\frac{\partial \boldsymbol{G}_h}{\partial y}\, vdxdy-\int_{\Omega_e}\boldsymbol{Q}\, vdxdy=0 \tag{3.4}$$

Deriving by parts, the weak form of the DG discretization can be found:

$$\int_{\Omega_e}\frac{\partial u_h}{\partial t}\, v dx\, dy+\int_{\partial\Omega_e}(\hat{F}_h n_x+\hat{G}_h n_y)\, v ds-\int_{\Omega_e}\left(\frac{\partial v}{\partial x}F_h+\frac{\partial v}{\partial y}G_h\right)dx\, dy-\int_{\Omega_e}Q\, v dx\, dy=0 \tag{3.5}$$

where $\partial\Omega_e$ is the boundary curve of the element, $n_x$ and $n_y$ are the component of the unit normal vector which points outward the element. In order to perform the integral on $\partial\Omega_e$ , the fluxes $\hat{F}_h$ and $\hat{G}_h$ at the interface of the neighbouring cells must be known. Their contributions are calculated separately following the procedure described in [6].

Equation 3.5 must be valid for $\forall\, v$ since the equation is valid for all $N_e$ functions which define the element basis. Setting for example $v=\Psi_i$ with $1\leq i\leq N_e$ , $N_e$ equations can be obtained and used in order to describe the evolution in time of the $N_e$ solution coefficients inside the cell $\Omega_e$.

$$\int_{\Omega_e} \frac{\partial u_h}{\partial t} \Psi_i \Psi_j \, dx\, dy + \int_{\partial\Omega_e} (\hat{F}_h n_x + \hat{G}_h n_y) \Psi_j \, ds - \int_{\Omega_e} \left( \frac{\partial \Psi_j}{\partial x} F_h + \frac{\partial \Psi_j}{\partial y} G_h \right) dx\, dy + \\ - \int_{\Omega_e} Q \Psi_j \, dx\, dy = 0 \qquad 1 \le j \le N_e \tag{3.6}$$

That system can be written in compact form introducing the mass matrix [**M**] of the element defined as:

$$[\boldsymbol{M}_{(ij)}] = \int_{(\Omega_e)} \Psi_i \Psi_j \, dx\, dy \tag{3.7}$$

$$[\boldsymbol{M}] \frac{\partial \tilde{\boldsymbol{u}}}{\partial t} = - \int_{\partial\Omega_e} (\hat{F}_h n_x + \hat{G}_h n_y) \boldsymbol{\Psi} \, ds + \int_{\Omega_e} \left( \frac{\partial \boldsymbol{\Psi}}{\partial x} F_h + \frac{\partial \boldsymbol{\Psi}}{\partial y} G_h \right) dx\, dy + \int_{\Omega_e} Q \boldsymbol{\Psi} \, dx\, dy \tag{3.8}$$

which is the discontinuous Galerkin semidiscrete formulation which describes the evolution in time of the degree of freedom of the element.

For mapping, choice of the basis, recovery method and further information, the reader can consult [6].

# Chapter 4 - Time discretization

Recalling equation 3.8, the system of equation for all elements in the domain is described by:

$$[\underline{M}]\frac{d\tilde{\boldsymbol{u}}}{dt}=-\underline{R}(\tilde{\boldsymbol{u}}) \tag{4.1}$$

where $[\underline{M}]$ is the diagonal global mass matrix, $\tilde{\boldsymbol{u}}$ is the global vector of degrees of freedom and $R(\tilde{\boldsymbol{u}})$ is the global vector of residuals which is derived by the boundary and volume integrals of the last equation of the previous chapter.

Considering a general convection-diffusion problem, the stability limits are computed separately in each cell and defining *CFL*, *c*, *κ*, $H_e$ and $p_e$ as respectively the stability coefficient, maximum signal speed, diffusivity coefficient and element characteristic size and order, results that:

$$\Delta t_d=CFL\frac{H_e^2}{\kappa(2p_e+1)} \tag{4.2}$$

$$\Delta t_c=CFL\frac{H_e}{c(2p_e+1)} \tag{4.3}$$

After that, the minimum time step of all domain cells is identified and used as global time step.

Now, a new notation is introduced in order to to simplify the further discussion. In particular, a reference problem which is described by ordinary differential equations in considered:

$$\frac{d\boldsymbol{u}}{dt}=L(\boldsymbol{u}) \tag{4.4}$$

## 4.1 - Explicit Runge-Kutta methods

A first order accuracy for time integration is reached using the Forward Euler method:

$$\boldsymbol{u}^{n+1}=\boldsymbol{u}^{n}+\Delta t\, L(\boldsymbol{u}^{n}) \tag{4.5}$$

Since using this method some problems containing discontinuities give spurious oscillations in results connected to time integration, a two and three stages Total Variation Diminishing Runge-Kutta (TVD RK) were implemented [9].

Second-order two stages TVD-RK can be written as follow:

$$\boldsymbol{u}^{(1)}=\boldsymbol{u}^{n}+\Delta t\, L(\boldsymbol{u}^{n}) \tag{4.6}$$

$$\boldsymbol{u}^{n+1}=\frac{1}{2}\boldsymbol{u}^{n}+\frac{1}{2}\boldsymbol{u}^{(1)}+\frac{1}{2}\Delta t\, L(\boldsymbol{u}^{(1)}) \tag{4.7}$$

Instead the third-order three stages TVD-RK has the form:

$$\boldsymbol{u}^{(1)}=\boldsymbol{u}^{n}+\Delta t\, L(\boldsymbol{u}^{n}) \tag{4.8}$$

$$\boldsymbol{u}^{(2)}=\frac{3}{4}\boldsymbol{u}^{n}+\frac{1}{4}\boldsymbol{u}^{(1)}+\frac{1}{4}\Delta t\, L(\boldsymbol{u}^{(1)}) \tag{4.9}$$

$$\boldsymbol{u}^{n+1}=\frac{1}{3}\boldsymbol{u}^{n}+\frac{2}{3}\boldsymbol{u}^{(2)}+\frac{2}{3}\Delta t\, L\left(\boldsymbol{u}^{(2)}\right) \tag{4.10}$$

In all simulation performed a second-order accuracy in time is reached, so the second order TVD-RK is used in body fitted simulations of this work. In order to reach higher order accuracy in time integration, see [6].

## 4.2 - Implicit method

Also the implicit Backward Euler (BE) method was used in this work, specificly concerning in test cases performed with IB method. Recalling the equation

$$[\underline{M}]\frac{d\tilde{\boldsymbol{u}}}{dt}=-\underline{R}(\tilde{\boldsymbol{u}})$$

The BE formulation can be obtained linearizing the previous equation, resulting

$$[\underline{M}]\frac{\tilde{\boldsymbol{u}}^{n+1}-\tilde{\boldsymbol{u}}^{n}}{\Delta t}=-\left(\underline{R}(\tilde{\boldsymbol{u}})^{n}+[\underline{J}](\tilde{\boldsymbol{u}}^{n+1}-\tilde{\boldsymbol{u}}^{n})\right) \tag{4.11}$$

where $[\underline{J}]$ is the jacobian matrix and $[\underline{M}]$, as said, is the global mass matrix. It is a block diagonal matrix. A single block is obtained by an element mass matrix. Instead, the jacobian matrix is a block sparse matrix which is defined by the derivatives of the residuals with respect to the degree of freedom:

$$\underline{J}_{ij}=\frac{\partial \underline{R}_i}{\partial \tilde{u}_j}\quad .$$

The equation can be written in compact form in order to evidence the linear system given by

$$\left(\frac{1}{\Delta t}[\underline{M}]+[\underline{J}]\right)(\tilde{\boldsymbol{u}}^{n+1}-\tilde{\boldsymbol{u}}^{n})=-\underline{R}(\tilde{\boldsymbol{u}}^{n}) \tag{4.12}$$

$$[\boldsymbol{A}](\tilde{\boldsymbol{u}}^{n+1}-\tilde{\boldsymbol{u}}^{n})=-\underline{R}(\tilde{\boldsymbol{u}}^{n}) \tag{4.13}$$

which must be solved at each time step since $\tilde{\boldsymbol{u}}$ must be updated. Here, $\tilde{\boldsymbol{u}}$ is the global vector of degrees of freedom which has size $M\sum_{i=1}^{n_{ele}} N_i$, where $M$, $n_{ele}$, and $N_i$ are respectively the number of governing equations, the element number and the number of degrees of freedom in i-element [6].

# Chapter 5 - Profile generation

## 5.1 - Roots' profile generation

Among positive displacement lobe machine, roots blowers are the oldest in used. In fact, they are used since 1860. Roots compressor are the precursor of screw compressor since they pump fluid with two meshing rotors. The differences between roots and screw compressor are in profile shape, number of lobes and the axial geometry. In fact, roots compressor are not twisted in axial direction as screw compressors. This reflects on the direction of compression: roots compressors pump fluid in transversal direction unlike screw compressors which pump fluid in axial direction.

Typical roots blower has cycloidal rotors constructed starting from hypocicloidal and epycicloidal curves. A rotor which contains two lobes is generated starting from circles having one-quarter the diameter of the larger. Instead, real roots blower have more complex geometries to improve the efficiency. Since the two rotors have to maintain a clearance between them, a single stage root blower can work in a limited pressure ratio range.

Roots rotor's profile used in this work is represented in Fig. 2.Profile points are obtained by extrapolation from a vector image of a two-lobe roots profile of public domain which can be found in [10]. Points are extracted with the software [11]. After that, inter-axis length is calculated and profiles are adimensionalized using that length.

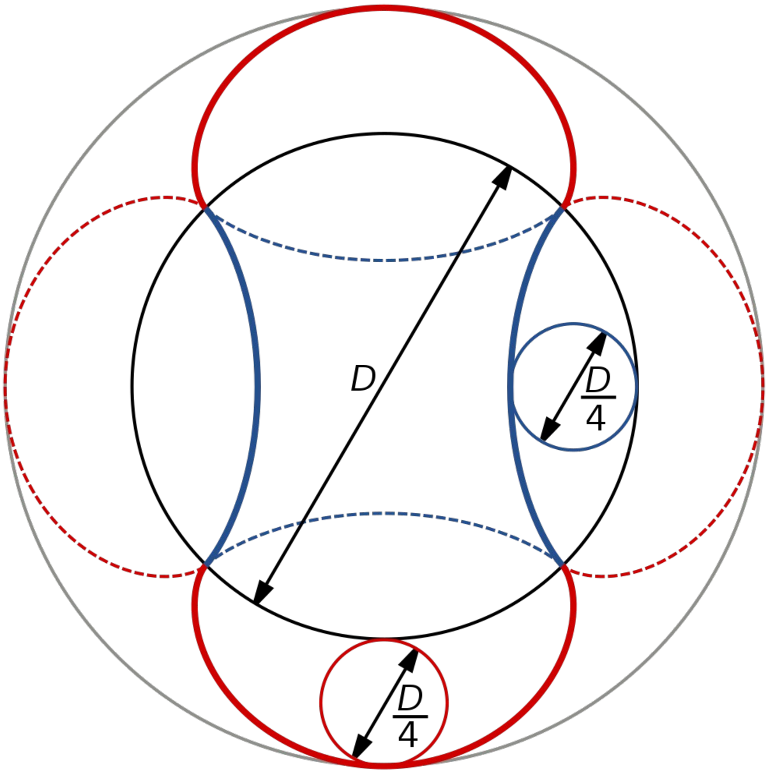


*Figure 2: Involute profile of two-lobes roots rotor*

## 5.2 - Historical development of screw compressors' profile

Rotor profile of the screw compressor affects significantly their performances. Habitually a tooth profile is generated starting from different types of curve for main rotor and then conjugate curves are generated on the gate rotor.

First appearance in literature of a screw compressor dates back in 1939 by the patent of Alf Lysholm [12]. It was produced and commercialized by Svenska Rotor Maskiner (SRM), a Swedish company. It kept under industrial secret their design techniques and parameters. Consequently, since profiling parameters were not know, few developments on screw compressor profile design were carried out in Europe and U.S.A. Most of publications unfortunately were limited in numeric parameters since the authors were employees in compressor producing company who did not want to share their knowledge.

Opposite to this company politics, three textbooks on screw machines were published in Russia. Here, there was the need to develop design procedures from the beginning, since there were not patent regulation with European and American companies. Sakun (1960) [13] fully described a rotor profile generation with circle, ellipse, and cycloid, and, most relevant, a consistent representation of profile characterized by geometrical asymmetry properties, called later SKBK. An envelop approach is used in this book in order to generate the tooth profile. Andreev (1961) [14] repeated what Sakun made before concerning profile development giving his contribution adding manufacturing and tooling information . Two decades after, in 1977, Amosov et al. [15] resumed Sakun's work improving it with his own contribution consisting on the presentation, for the first time in the public literature, of a reproducible method in order to generate the classic Lysholm's SMR asymmetric profiles. This book was translated into German and English where possible.

Two textbooks on screw machines were published in Germany. *Rinder* (1979) [16] used gear theory to reproduce the SMR asymmetric profile. *Konka* [17] gave his contribution disclosing some engineering aspects of screw compressors, but his profiling procedures are not simple reproducible. *Rinder*'s book was also translated in English. There are two textbooks published in English which handle some aspects of screw compressor: *O'Neil* (1993) [18] concerning industrial compressor, and *Arbon* (1994) [19] treating rotaty twin shaft compressor, but none of them gives sufficient indication of rotor profiling procedures, neither generally. There are not many compressor manufactures' handbooks on screw machines and brochures which give useful information on them are either classified or available only under licensing. At the beginning of the century, Xing (2000) [20] published in Chinese a practical textbook on screw compressors, and in 2005 and 2006, Stosic et al. [4] published a more comprehensive handbooks on screw machines only which deal with many aspects of them, but also in this case, the profiling process is poor of details.

As profiling is concerned, a large number of licensees are present. The SMR in 1952 symmetric profile by *Nilson* [21], 1979, asymmetric profile by

*Shibbie* [22], *Astberg* [23] in 1982 with “D” and *Ohman* (1999) [24] with “G” profiles are typical examples, but also other profiles developed by companies were also very successful. All profile described are , without doubt, generate by valid procedure, but insufficient data are given in order to make them reproducible in easy manner. [25]

In his textbook [4], Stosic described a pair of rack-generated rotors in order reduce Rinder’s profile large blow hole area. Stosic’s rotor profile is generated starting from several curves given in a general implicit form: $ax^p+by^q=1$ . This generated rotor is the first which can be used to improve rotor profile performances. Unfortunately, details about undercut limits and numeric parameters are not publically available. In fact parameters such as *a, b, p* and *q* in previous equation in implicit form are not well defined enough for rotor profile modification. Therefore, Wu et al.[26] describe a rack profile method with well defined parameters and equations in explicit forms from Stosic’s patent [27], known also as “N” profile, to generate a pair of conjugated rotors which can be easily modify in order to improve compressor performance.

Unfortunately [26] contains wrong parameters, since it notices that undercut limit in male-profile parameters is overcome. The work of, [28], contains wrong explicit equations and parameters, since the basic rack profile can not be even drawn. These errors surely are due to mistake in typing. The following section provides the exact equations and parameters through which the profile, used in this work, has been generated, resuming and correcting the work done by Wu et al. [28].

# 5.3 - Mathematical model

## 5.3.1 - Explicit equation of rack generator

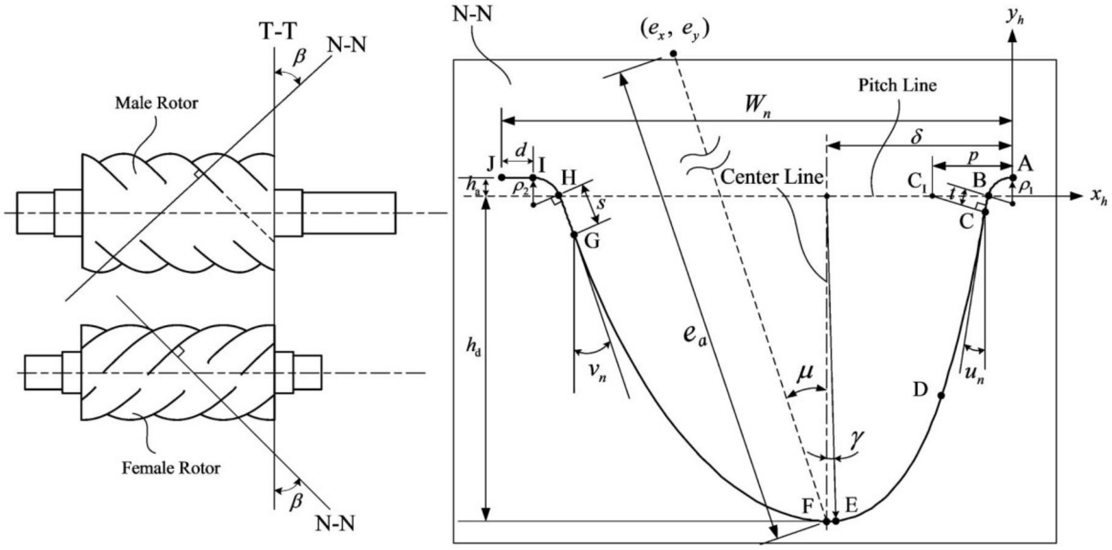


*Figure 3: Rack and its functional parameters [28]*

The fundamental parameters from which the tooth profile is constructed are the center distance between rotor axes $A_c$, the lobes number of male and female rotors $z_1$ and $z_2$ , the inner radii of the male and female rotors $r_{d1}$ and $r_{d2}$, and the outer radii of the male and female rotors $r_{o1}$ and $r_{o2}$. Others relevant parameters are the normal circular pitch $W_n$ and the total tooth height ($h_a$+$h_d$).

As shown in Fig. 1, the addendum $h_a$, the dedendum $h_d$, and the normal circular pitch $W_n$ can be determined by the following equations:

$$r_{p1}=z_1 A_c/(z_1+z_2)$$

$$r_{p2}=z_2 A_c/(z_1+z_2)$$

$$h_a = r_{p1} - r_{d1} = r_{o1} - r_{p2}$$

$$h_d = r_{o1} - r_{p1} = r_{p2} - r_{d2}$$

$$W_n = W_t \cos\beta = (2\pi r_{p1}/z_1)\cos\beta = (2\pi r_{p2}/z_2)\cos\beta$$

where $\beta$ is the helix angle at the pitch circle, $W_t$ is the transverse circular pitch, and $r_{p1}$ and $r_{p2}$ are the pitch radii respectively of the male and female rotors. The generator curves $\boldsymbol{r}(\theta)$ are listed in Table 1. The unit normal vector $\boldsymbol{n}(\theta)$ of the curve segments can be derived from the following equation:

$$\boldsymbol{n}(\theta) = \frac{\boldsymbol{k} \times \partial_\theta \boldsymbol{r}(\theta)}{|\boldsymbol{k} \times \partial_\theta \boldsymbol{r}(\theta)|}$$

where $\boldsymbol{k}$ is the unit vector of the z-direction defined as $\boldsymbol{k}=(0, 0, 1)^T$.

*Table 1: Explicit equations of the normal rack [26]*

| Rack | | | |
|---|---|---|---|
| **Segment** | **Type** | **Explicit equations** | **Range** |
| AB | Circular arc | $\boldsymbol{r}_1 = \begin{cases} x_1(\theta) = -\rho_1 \sin\theta \\ y_1(\theta) = h_a - \rho_1(1-\cos\theta) \end{cases}$ | $0 \le \theta \le \frac{\pi}{2} - u_n$ |
| BC | Straight line | $\boldsymbol{r}_2 = \begin{cases} x_2(\theta) = x_1\left(\frac{\pi}{2} - u_n\right) - \theta \sin u_n \\ y_2(\theta) = y_1\left(\frac{\pi}{2} - u_n\right) - \theta \cos u_n \end{cases}$ | $0 \le \theta \le t$ |

| | | | |
|---|---|---|---|
| CD | Normal equidistant trochoid | $\boldsymbol{r}_3=\begin{cases} x_3(\theta)=\left[K_1(\theta)-\dfrac{\kappa K_1(\theta)}{\sqrt{K_1(\theta)^2+K_2(\theta)^2}}-(p+r_{p2}\theta)\right]\cos\beta \\ y_3(\theta)=K_2(\theta)-\dfrac{\kappa K_2(\theta)}{\sqrt{K_1(\theta)^2+K_2(\theta)^2}} \end{cases}$ | $0\le\theta\le\zeta$ |

$$C_x=x_2(t)/\cos\beta$$

$$C_y=y_2(t)$$

$$u_t=\arctan(\tan u_n/\cos\beta)$$

$$K_1(\theta)=(C_x+p)\cos\theta+\kappa\cos(u_t+\theta)+(C_y+r_{p2})\sin\theta$$

$$K_2(\theta)=-r_{p2}-(C_x+p)\sin\theta-\kappa\sin(u_t+\theta)+(C_y+r_{p2})\cos\theta$$

| | | | |
|---|---|---|---|
| DE | Normal equidistant trochoid | $\boldsymbol{r}_4=\begin{cases} x_4(\theta)=\left[K_3(\theta)+\dfrac{\tau K_3(\theta)}{\sqrt{K_3(\theta)^2+K_4(\theta)^2}}+(r_{p1}\theta-p-r_{p2}\zeta)\right]\cos\beta \\ y_4(\theta)=K_4(\theta)+\dfrac{\tau K_4(\theta)}{\sqrt{K_2(\theta)^2+K_4(\theta)^2}} \end{cases}$ | $0\le\theta\le\eta$ |

$$D_x=x_3(\zeta)/\cos\beta$$

$$D_y=y_3(\zeta)$$

$$h_x=D_x-\frac{\tau K_1(\zeta)}{\sqrt{K_1(\zeta)^2+K_2(\zeta)^2}}$$

$$h_y=D_y-\frac{\tau K_2(\zeta)}{\sqrt{K_1(\zeta)^2+K_2(\zeta)^2}}$$

| | | | |
|---|---|---|---|
| | | $K_3(\theta)=(p+r_{p2}\zeta+h_x)\cos\theta-(r_{p1}-h_y)\sin\theta$ | |
| | | $K_4(\theta)=r_{p1}-(p+r_{p2}\zeta+h_x)\sin\theta-(r_{p1}-h_y)\cos\theta$ | |
| EF | Circular arc | $\boldsymbol{r}_5=\begin{cases} x_5(\theta)=-\delta+h_d\sin\theta \\ y_5(\theta)=-h_d-\cos\theta \end{cases}$ | $0\le\theta\le\gamma$ |
| FG | Bias ellipse | $\boldsymbol{r}_6=\begin{cases} x_6(\theta)=(e_x-e_b\sin\theta)\cos\mu-(e_y-e_a\cos\theta)\sin\mu-\delta \\ y_6(\theta)=(e_y-e_a\cos\theta)\cos\mu-(e_x-e_b\sin\theta)\sin\mu \end{cases}$ | $\theta_1\le\theta\le\theta_2$ |
| GH | Straight line | $\boldsymbol{r}_7=\begin{cases} x_7(\theta)=x_8\left(\frac{\pi}{2}-v_n\right)-\theta\sin v_n \\ y_7(\theta)=y_8\left(\frac{\pi}{2}-v_n\right)-\theta\cos v_n \end{cases}$ | $0\le\theta\le s$ |
| HI | Circular arc | $\boldsymbol{r}_8=\begin{cases} x_8(\theta)=x_9(d)+\rho_2\sin\theta \\ y_8(\theta)=y_9(d)-\rho_2(1-\cos\theta) \end{cases}$ | $0\le\theta\le\frac{\pi}{2}-v_n$ |
| IJ | Straight line | $\boldsymbol{r}_9=\begin{cases} x_9(\theta)=-W_n+\theta \\ y_9(\theta)=h_a \end{cases}$ | $0\le\theta\le d$ |

According to Fig. 1, the 11 rack parameters, $\rho_1$, $\rho_2$, $u_n$, $v_n$, $t$, $s$, $\kappa$, $\tau$, $d$, $\gamma$, and $e_a$, are defined on the normal-rack segments. The parameters $\rho_1$ and $\rho_2$, which represent the radii of the circular arcs AB and HI, respectively, are used to define the tooth top-land shape of the female rotor. Parameters $u_n$ and $v_n$, which represent the normal pressure angles on the high- and low-pressure sides, respectively, are used to adjust the direction of sealing near the pitch circle. Parameters $t$ and $s$, which represent the length of the straight lines BC and GH, respectively, are used to modify the length of the involutes of the rotor profiles. Parameters $\kappa$ and $\tau$, which represent normal equidistances of the trochoids CD and DE, respectively, are used to adjust the radii of the rotor tooth flanks on the high-pressure side. Parameter $d$, which represents the length of the straight line IJ, is used to adjust the tooth thickness of the female rotor. Parameter $\gamma$ is used to define the protection arc on the tip of the male rotor. Finally, parameter $e_a$ is the major radius of the bias ellipse FG that determines the curvature and contact length of the tooth flank on the low-pressure side. In addition, the consecutive curve segments are smoothly connected; that is, the unit normal vector **n** and the position vector **r** are the same at the connecting points:

$$\begin{cases} \boldsymbol{n}_i = \boldsymbol{n}_{i+1} \\ \boldsymbol{r}_i = \boldsymbol{r}_{i+1} \end{cases}, \quad i = 1 - 8 \tag{5.1}$$

The eight unknowns $p$, $\zeta$, $\eta$, $\delta$, $\mu$, $e_x$, $e_y$, and $e_b$ can be solved using the above equations with the following predetermined parameters: the center distance, the number of lobes, the diameters of the outer circles the diameters of the inner circles and the 11 profile parameters. The dataset of parameters listed in Tables 2 is used to generate the profile [28].

*Table 2: Input data of designed screw rotors [28]*

| **No.** | **Item** | **Symbol** | **Example** | **Units** |
|---|---|---|---|---|
| 1 | Lobe number of male rotor | $z_1$ | 5 | - |
| 2 | Lobe number of female rotor | $z_2$ | 6 | - |
| 3 | Center distance between rotor axes | $A_c$ | 80.02 | mm |
| 4 | Outer radius of male rotor | $r_{o1}$ | 56.5475 | mm |
| 5 | Outer radius of female rotor | $r_{o2}$ | 44.8112 | mm |
| 6 | Inner radius of | $r_{d1}$ | 35.2088 | mm |

| | | | | |
|---|---|---|---|---|
| | male rotor | | | |
| 7 | Inner radius of female rotor | $r_{d2}$ | 23.4725 | mm |
| 8 | Helix angle at rotor pitch circle | $\beta$ | 46.0 | deg |
| 9 | Length of rotor | $L$ | 183.068 | mm |

*Table 3: Design data of the normal rack [28]*

| No. | Symbol | Example | Units |
|---|---|---|---|
| 1 | $\rho_1$ | 1.675 | mm |
| 2 | $\rho_2$ | 3.255 | mm |
| 3 | $u_n$ | 6.291 | deg |
| 4 | $v_n$ | 17.776 | deg |
| 5 | $t$ | 0.8 | mm |
| 6 | $s$ | 0.878 | mm |
| 7 | $\kappa$ | 1.323 | - |
| 8 | $\tau$ | 1.983 | - |
| 9 | $d$ | 0.8 | mm |
| 10 | $\gamma$ | 0.718 | deg |
| 11 | $e_a$ | 35.1459 | mm |
| 12 | $W_n$ | 31.7509 | mm |
| 13 | $p$ | 9.5974 | mm |
| 14 | $\zeta$ | 0.5671 | - |
| 15 | $\eta$ | 0.5095 | - |
| 16 | $\delta$ | 11.1190 | mm |
| 17 | $\mu$ | -0.0331 | rad |
| 18 | $e_x$ | 0.3187 | mm |

| | | | |
|---|---|---|---|
| 19 | $e_y$ | 14.9764 | mm |
| 20 | $e_b$ | 19.2518 | mm |
| 21 | $\theta_1$ | -0.0181 | - |
| 22 | $\theta_2$ | 1.0511 | - |

## 5.1.2 - Rack-generated rotor profile

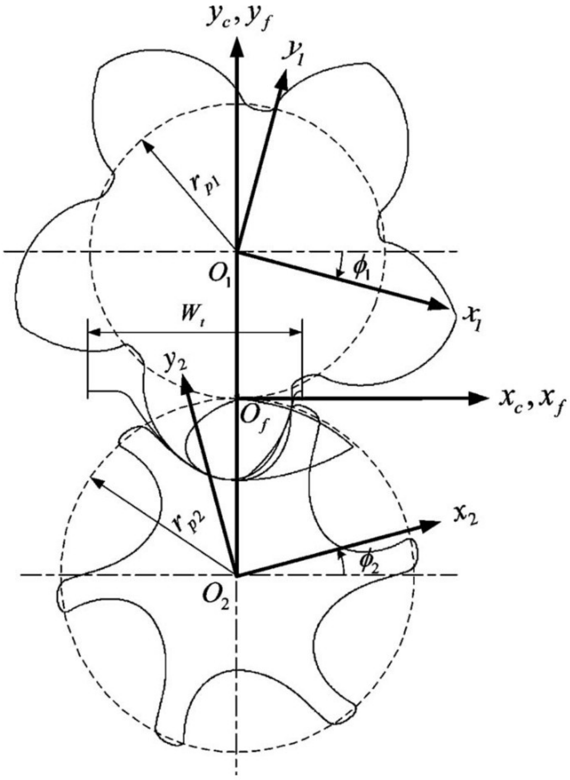


*Figure 4: Coordinate systems applied to rack-generated rotor profiles [26]*

As shown in Fig. 2, the lobe profile of male rotor is generated by normal rack in transverse plane of the rotor. The rack locus can be derived in coordinate system $S_{1,}$, which is rigidly attached to the male rotor, as given in the following:

$$male\,rotor = \begin{cases} x_m(\theta,\phi_1) = (x_c - s_c)\cos\phi_1 - (y_c - r_{p1})\sin\phi_1 \\ y_m(\theta,\phi_1) = (x_c - s_c)\sin\phi_1 + (y_c - r_{p1})\cos\phi_1 \end{cases} \tag{5.2}$$

$$female\,rotor = \begin{cases} x_f(\theta,\phi_2) = (x_c - r_{p2}\phi_2)\cos\phi_2 + (r_{p2} + y_c)\sin\phi_2 \\ y_f(\theta,\phi_2) = (r_{p2} + y_c)\cos\phi_2 - (x_c - r_{p2}\phi_2)\sin\phi_2 \end{cases} \tag{5.3}$$

where $\Phi_1$ is the rotation angle of the male rotor, $\Phi_2 = z_1\Phi_1/z_2$ is the rotation angle of the female rotor, $s_c = r_{p1}\,\Phi_1$ is the rack displacement, and the position vector in the rack coordinate system $S_c$ can be represented as

$$\boldsymbol{r}_c = [x_c, y_c] = [(x_h + \delta)/\cos\beta, y_h] \quad .$$

The relationship between the profile parameter $\theta$ and the rotation angle $\Phi$ can be found by the so-called equation of meshing in the theory of gearing [29]. At the tangent point between the rack locus and the tooth profile of the male rotor, the common normal vector $\boldsymbol{n}_h$ should be perpendicular to the relative sliding velocity between the rack and the male rotor $\boldsymbol{V}_{c1}$. Thus, the equation of meshing for the male rotor is as follows:

$$f_{m1} = (\theta,\phi_1) = \boldsymbol{n}_h(\theta)\cdot\boldsymbol{V}_{c1}(\theta,\phi_1) = -n_{xh}y_c + n_{yh}(x_c - r_{p1}\phi_1) = 0 \tag{5.4}$$

where the relative velocity between the rack and the male rotor ca be written as $\boldsymbol{V}_{c1} = -y_c\omega_1\boldsymbol{i} + (x_c - r_{p1}\phi_1)\omega_1\boldsymbol{j}$ in the coordinate system $S_c$, and $\omega_1$ is the rotation speed of the male rotor.

The equation of meshing for the female rotor can be written as follows:

$$f_{m2} = (\theta,\phi_1) = \boldsymbol{n}_h(\theta)\cdot\boldsymbol{V}_{c2}(\theta,\phi_2) = n_{xh}y_c + n_{yh}(r_{p2}\phi_2 - x_c) = 0 \tag{5.5}$$

where the sliding velocity between the rack and the female rotor ca be written as $\boldsymbol{V}_{c2}=y_c\,\omega_2\,\boldsymbol{i}+(r_{p2}\,\phi_2-x_c)\,\omega_2\,\boldsymbol{j}$ in the coordinate system $S_c$ and $\omega_2$ is the rotation speed of the female rotor.

From meshing equation of male rotor 5.4, $\Phi_1$ is founded and substituted in the “male rotor”-equations 5.2 to obtain the male rotor profile equation in the following form:

$$\begin{cases} x_m=(n_{xh}/n_{yh})\,y_c\cos\phi_1+(r_{p1}-y_c)\sin\phi_1 \\ y_m=(n_{xh}/n_{yh})\,y_c\sin\phi_1-(r_{p1}-y_c)\cos\phi_1 \end{cases},\quad \phi_1=\frac{n_{yh}\,x_c-n_{xh}\,y_c}{n_{yh}\,r_{p1}} \tag{5.6}$$

Similarly, $\Phi_2$ is founded from the female meshing equation 5.5 and substituted in the “female rotor”-equations 5.3 to obtain the female rotor profile equation in the following form:

$$\begin{cases} x_f=(n_{xh}/n_{yh})\,y_c\cos\phi_2+(r_{p2}+y_c)\sin\phi_2 \\ y_f=-(n_{xh}/n_{yh})\,y_c\sin\phi_2+(r_{p2}+y_c)\cos\phi_2 \end{cases},\quad \phi_2=\frac{n_{yh}\,x_c-n_{xh}\,y_c}{n_{yh}\,r_{p2}} \tag{5.7}$$

For further details as sealing line, blow hole area or undercut limits see [26], [28], [30].

# Chapter 6 - Validation test case

In order to check the accuracy and reliability of the used numeric method, some test cases were performed. In particular we considered the flow around a circular cylinder: both periodic conditions and impulsive acceleration are investigated at Re=100.

## 6.1 - Circular cylinder in cross flow

Among papers involving compressible flow around circular cylinder at low-Re regimes, [31] and [32] give useful information about references of old results and recent ones obtained with newest numerical method. Since in this work discontinuous Galerkin (DG) method is used, [31] was taken as reference for result comparisons.

This test case is characterized by Re=$10^2$ and M=0.2 in far-field. The domain is composed of a circular boundary, as described in [31]. The far-field distance form the body is equal to 50 cylinder's diameters with cylinder's diameter equal to 1.

Two types of simulations were carried out. The first solves the problem applying the simple Navier-Stokes equations with body fitted mesh. Three simulations were performed in this way. The domain was discretized with an unstructured body fitted mesh, each of them was refined with respect the previous one. Mesh is finer around the cylinder and along its wake in order to capture better the occurrence of the well known vortex shedding. The refinement is proportional to the characteristic length which characterizes each grid.

The second adopts immersed boundary technique which uses the penalization method. Also in this case three simulation were carried out reducing linearly the characteristic length of the mesh element. In such a simulation the domain is no more composed by two circumferences as before but only by a single circumference of 50D since embedded grid is used. In fact we are applying penalization and so the cylinder is no more defined by the mesh but by the level set. Domain is discretized with an unstructured mesh with mesh refinement where cylinder is supposed to be and its wake, as before. Furthermore, an explicit time integration was used in body fitted simulations with a CFL=0.3, instead, as far as immersed boundary simulations are concerned, an implicit integration method is used by setting CFL=50. This choice was done considering the oscillation period of the Lift coefficient of simulation with BF mesh. In fact CFL was set to 50 in order to have a significant number of point in each Lift oscillation, in particular almost 50 points in each oscillation period, in order not to lose information. This was done because of the stiffness of the penalization terms which can introduce strong limitation on the time step size.

In simulation concerning penalization method, the penalization factor was fixed $\eta$=0.01 since smaller values are not allowed by mesh size constraint.

In this way, six simulation were performed and compared one by one, since characteristic length, number of points along the boundary of cylinder (2000 points) and along the wake (1000 points) are the same. The only difference is that the cylinder in IB simulation is also meshed up. The figure below shows the six different meshes.

Since all simulations require a lot of time in order to reach periodic oscillations in drag and lift coefficient, a Mach number equal to $1.1*M_\infty$ was set as initial boundary condition on the top of cylinder. In this way the transient part is decreased significantly and the Von Karman vortex shedding develops quickly.

*Table 4: Mesh used in the test case simulations on fixed cylinder*

| **Immersed boundary mesh** | **Body fitted mesh** |
| --- | --- |
| 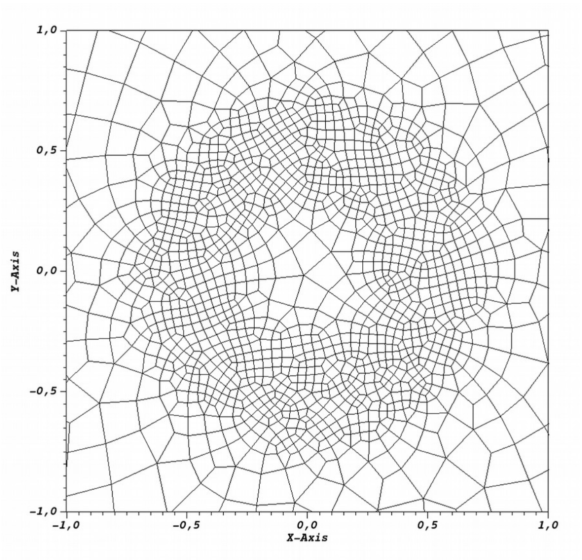 | 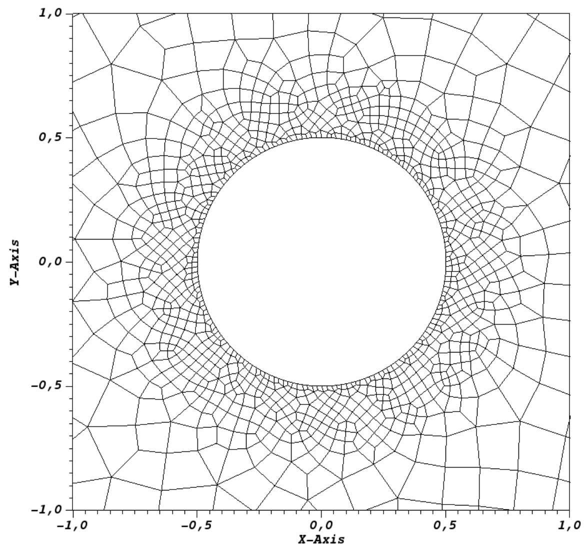 |
| 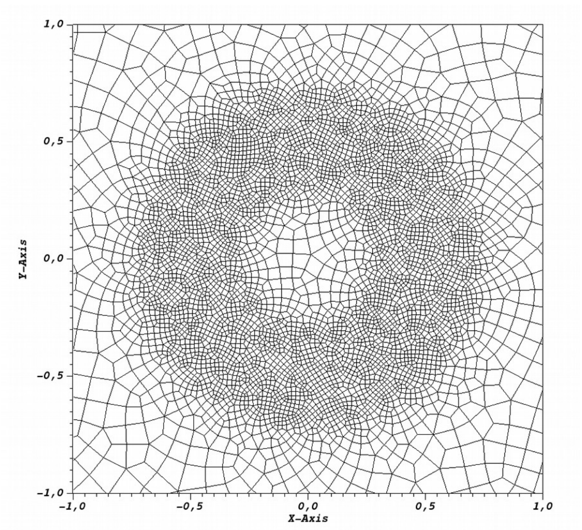 | 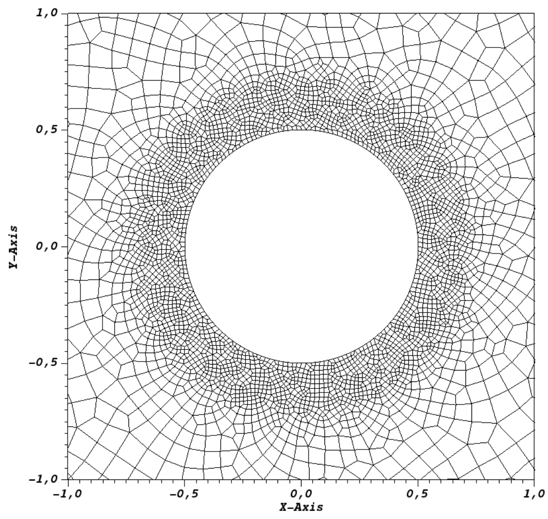 |

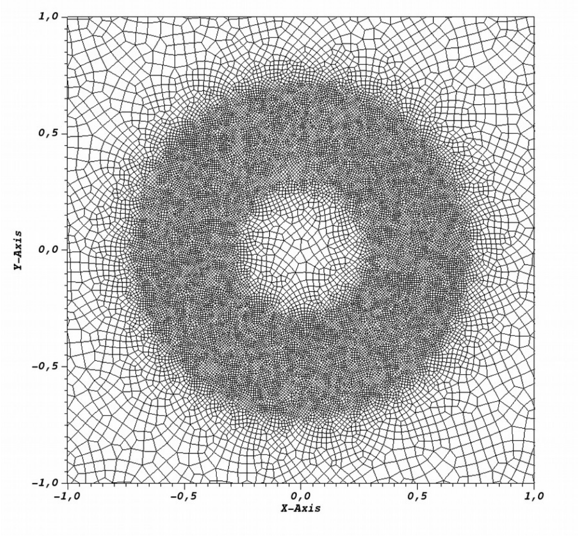


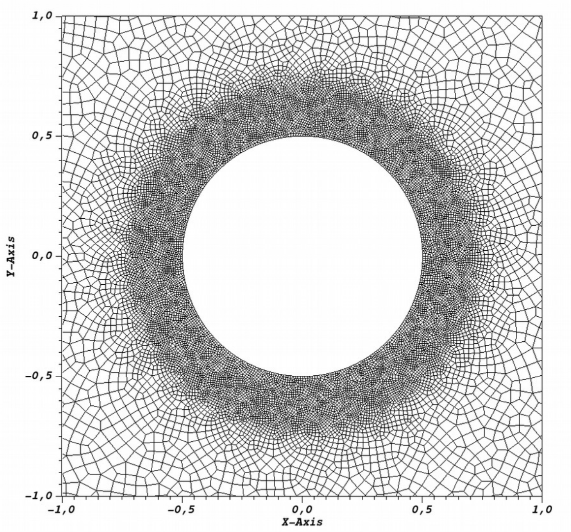


Results comparisons were made with Strouhal number St and mean drag coefficient $C_D$.

The Strouhal number (St) is related to vortex shedding. It is calculated as following :

$$St = \frac{f\,D}{u}$$

where *f*, *u*, *D* are adimensional quantities and correspond respectively to the frequency of shedding, the velocity of the free stream and the cylinder diameter.

Adimensional diameter D, as mentioned before, is equal to 1, the adimensional velocity is 0.2357. The adimensional frequency is calculated on 10 cycles of oscillation of the Lift coefficient $C_L$ defined as

$$C_L = \frac{F_L}{\frac{1}{2}\rho_\infty u_\infty^2 D}$$

where $F_L$, $\rho_\infty$, $u_\infty$, D are respectively force acting on cylinder in perpendicular direction with respect the flow which changes in time, adimensional density of the far-field equal to 0.9803, adimensional velocity of the far-field equal to 0.2357, adimensional diameter of cylinder equal to 1.

When the periodic regime is reached, the frequency is evaluated as $f=\frac{10}{t_2-t_1}$ . A typical trend is shown below.

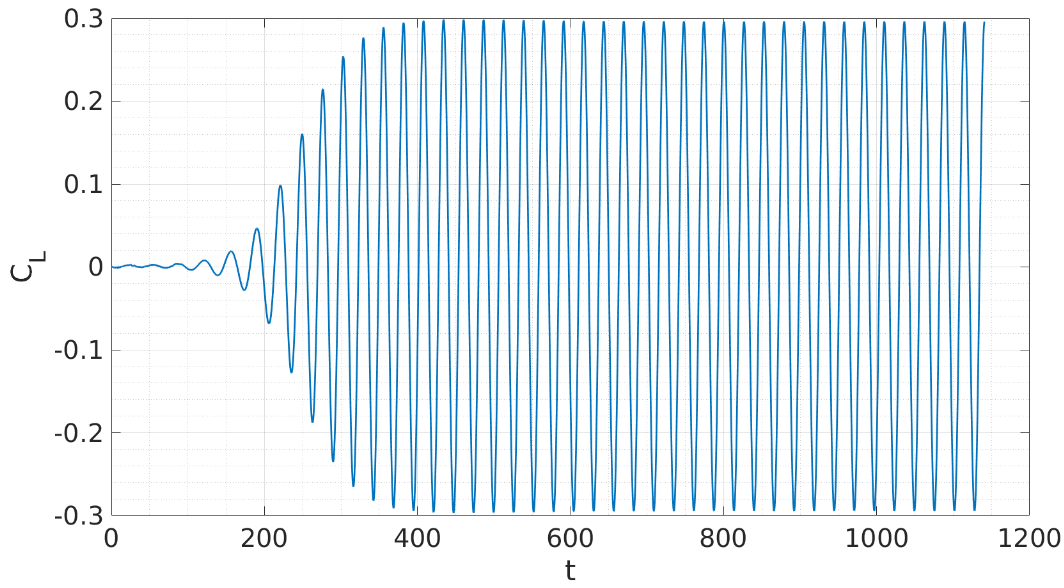


*Figure 5: Oscillation of Lift coefficient*

The mean drag coefficient is a measure of the drag forces acting on the cylinder. It is calculated as

$$C_D=\frac{F_D}{\frac{1}{2}\rho_\infty u_\infty^2 D}$$

where $F_D$, $\rho_\infty$, $u_\infty$, D are respectively the force acting on cylinder in parallel direction with respect the flow, adimensional density of the far-field, adimensiona velocity of the free stream, adimensional diameter of cylinder.

Also $C_D$ varies in time as $C_L$ and after it has reached periodicity, the mean value is calculates by a numerical integral average as $\bar{C_D} = \frac{\sum_{t_1}^{t_2} C_D(t_i)(t_i - t_{i-1})}{t_2 - t_1}$ where $C_D(t_i)$ is the value of $C_D$ at the time $t_i$. The typical trend of $C_D$ when periodicity is reached is shown below.

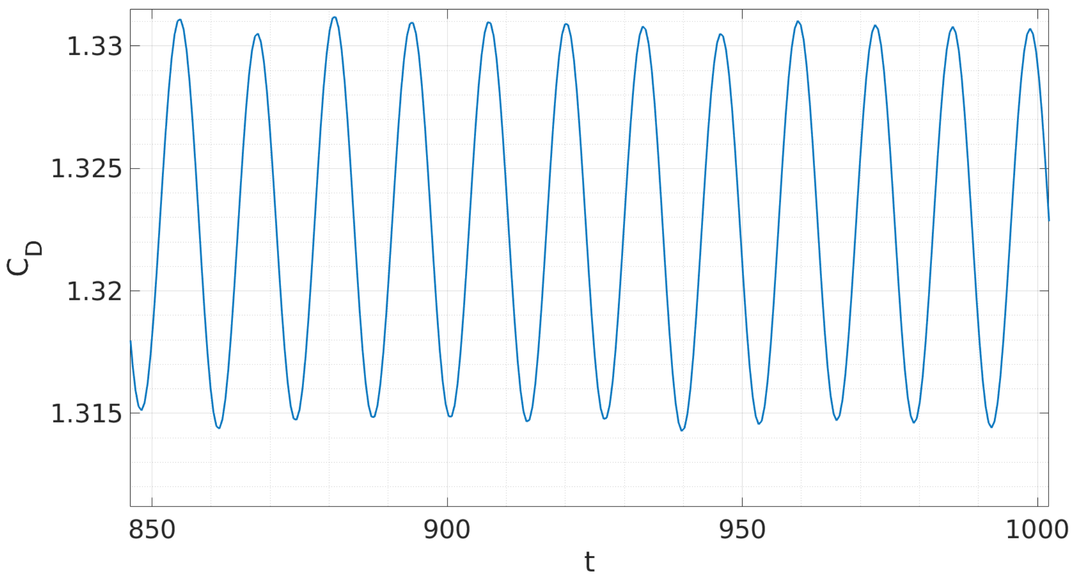


*Figure 6: Periodicity of Drag coefficient*

Note that there is an amplitude oscillations which seems periodic. This could be due to the fact that the domain is not infinite and so the flow around the cylinder is influenced by the position of the external boundaries and so the solution shows this kind of oscillation.

The domain was meshed with Gmsh. The main feature of the generated mesh is the *characteristic length* (lc) by which element size can be controlled. Starting from lc=20 it has been divided by a factor 2 twice.

The Table 5 summarizes the results obtained in terms of St and $C_D$.

*Table 5: Strouhal number and Drag coefficient obtained by the six simulation carried out in relation with the characteristic length used at Re=100 and M=0.2*

| **Cylinder characteristic length** | **Body fitted** | | **Immersed Bounday method** | |
|---|---|---|---|---|
| **lc** | **St** | **$C_D$** | **St** | **$C_D$** |
| 20 | 0.159 | 1.343 | 0.153 | 1.288 |
| 10 | 0.162 | 1.343 | 0.160 | 1.309 |
| 5 | 0.163 | 1.335 | 0.162 | 1.325 |

A list of values of St and $C_D$ is reported below which are used to demonstrate that the code gives consistent results.

*Table 6: Experimental results in literature for circular cylinder at Re=100*

| **Authors** | **Average $C_D$** | **St** |
|---|---|---|
| Norberg [33] | - | 0.164 |
| Tritton [34] | 1.26 | 0.157-0.164 |
| Wieselsberger [35] | 1.43 | - |
| Williamson [36] | 1.33 | 0.160-0.164 |
| Canuto [32] | 1.36 | 0.165 |
| Ferrero [31] | 1.33 | 0.163 |

It is possible to see that the result obtained with the presented method are in agreement with data available in literature. Especially, they fit very well with results obtained by Ferrero et al. Since the numerical method presented in this work is based on the one presented by Ferrero and the geometrical features of domain are almost the same, results in [31] are taken as reference values. So, a convergence study was performed and the results are reported below.

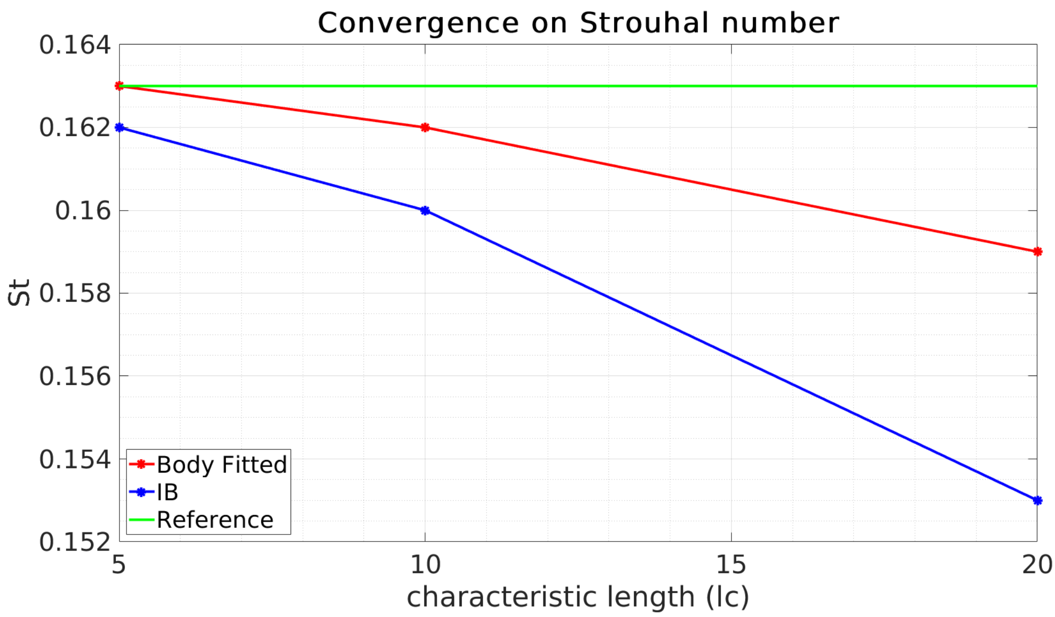


*Figure 7: Convergence of St over the characteristic length*

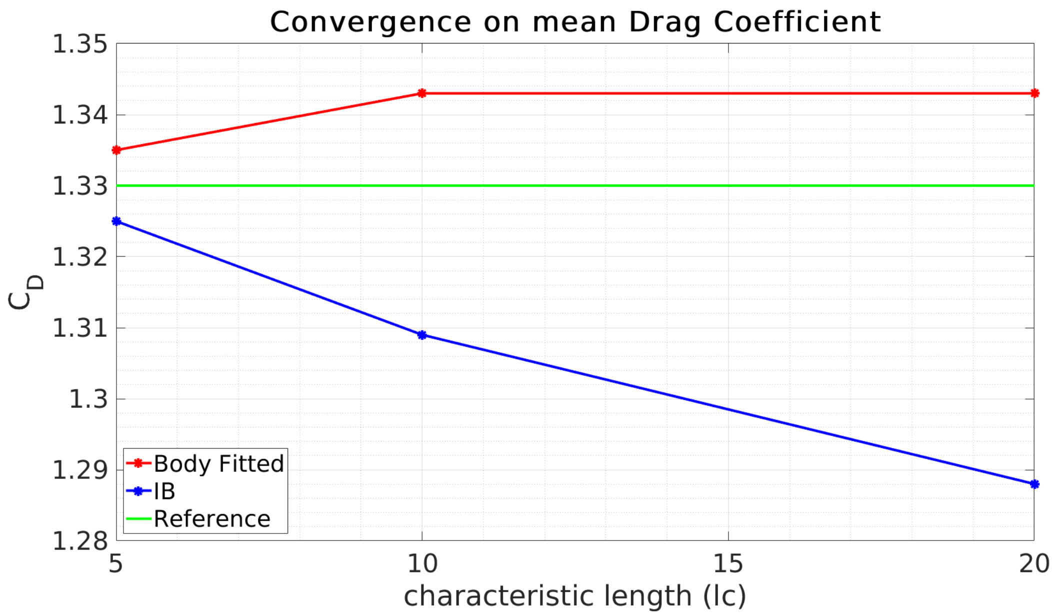


*Figure 8: Convergence of $C_D$ over characteristic length*

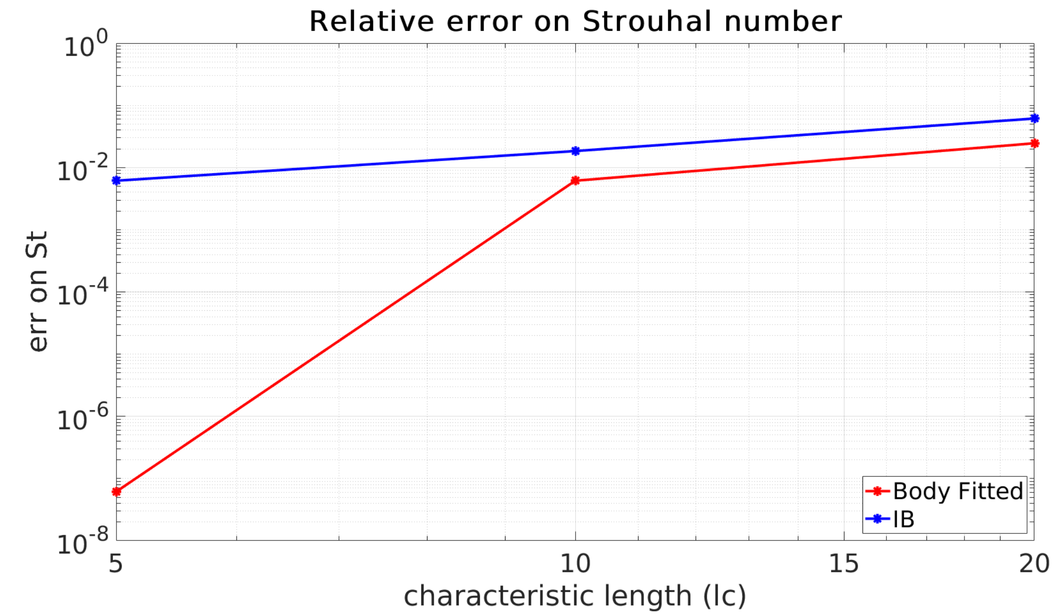


*Figure 9: Logarithmic trend of error on St*

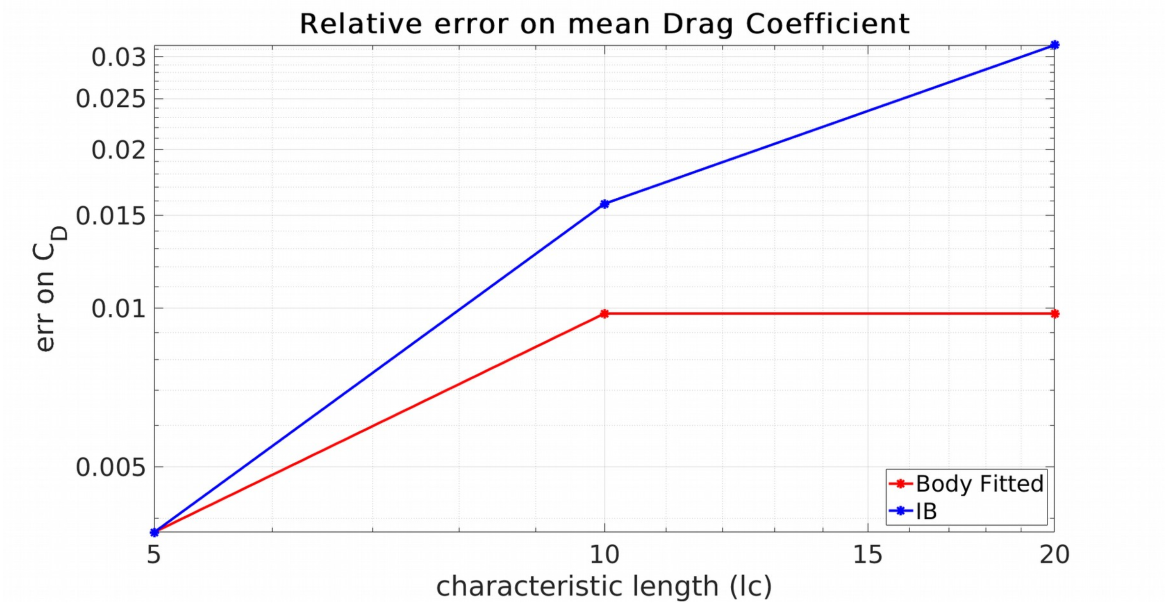


*Figure 10: Logarithmic trend of error on $C_D$*

It can be noted that body fitted simulations converge faster than IB simulations and they reach more accurate results than IB ones. This behavior is due to the fact that while in BF simulations the integral of $F_D$ and $F_L$ can be easily calculated since the boundary is well-known and smooth, in IB simulation it can not be done since the numerical grid has not smooth cylinder boundary. So, the integral is performed using the level set whose accuracy depends on the mesh size. In particular, the force on the body with the IB approach is computed by performing a volume integral of the penalized term which appears in the momentum equation. This leads to approximations in defining the cylinder shape on the numerical grid. Below is shown that the finest is the grid the more regular will be the shape of the cylinder.

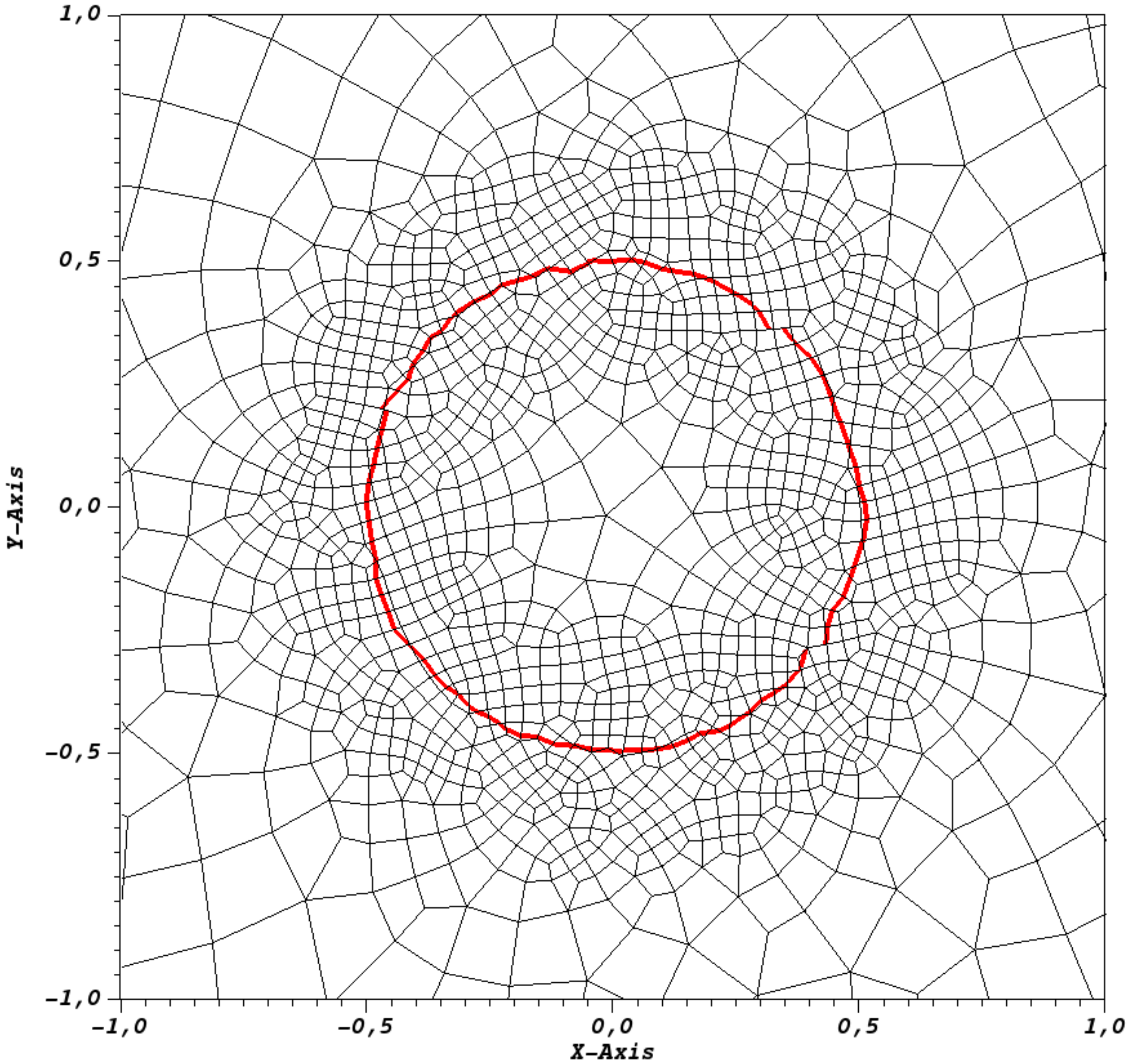


*Figure 11: Level set defining the cylinder in the first IB simulation*

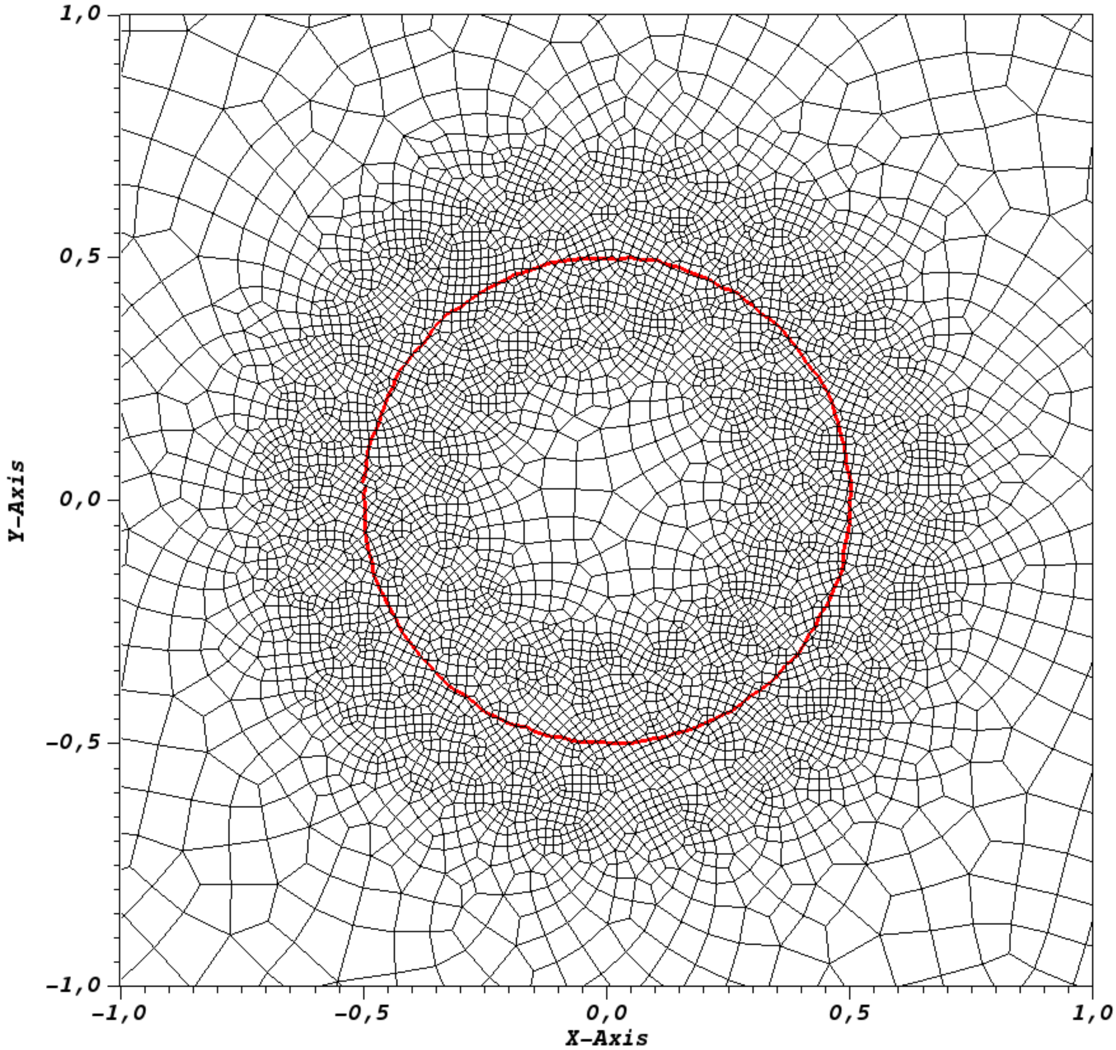


*Figure 12: Level set defining the cylinder in the second IB simulation*

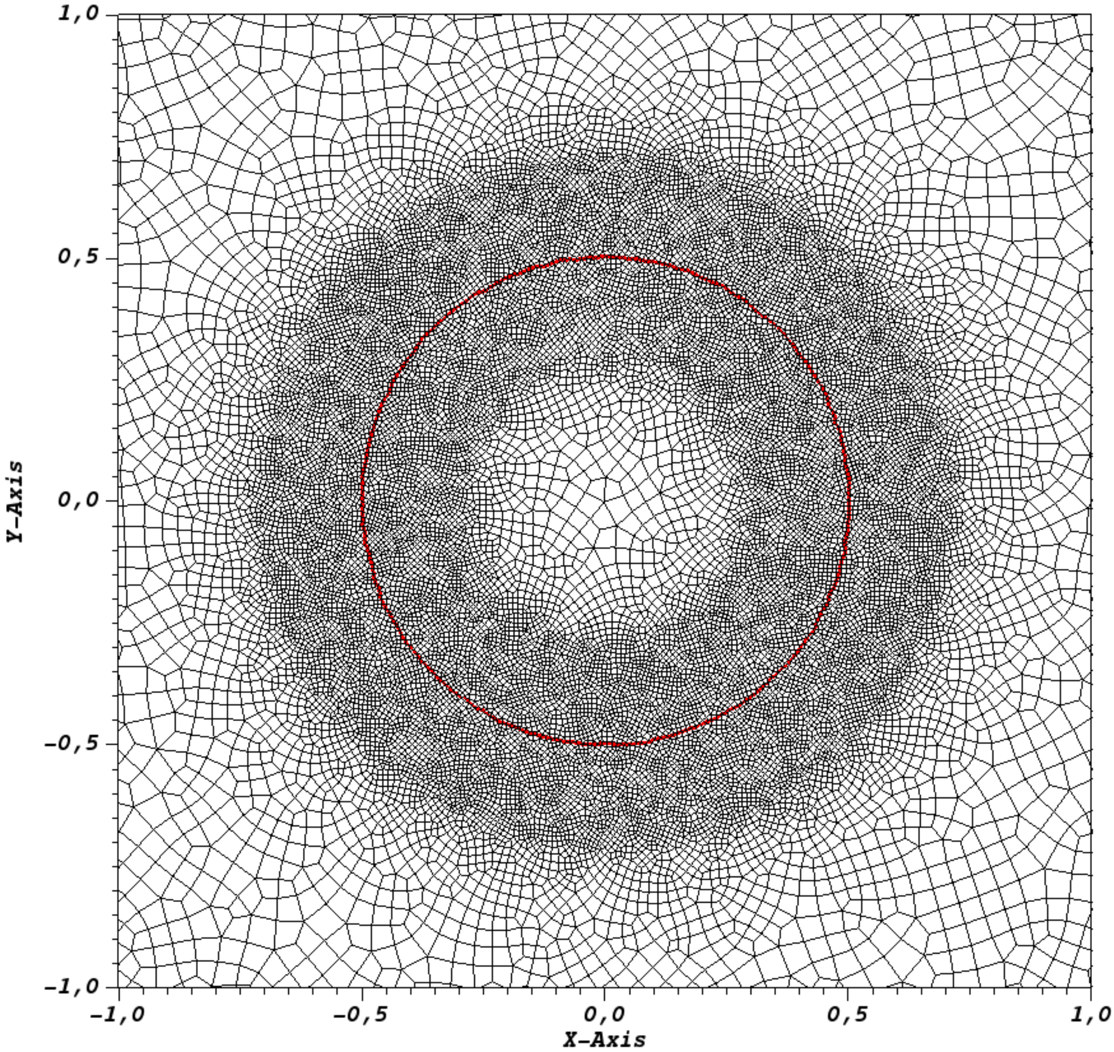


*Figure 13: Level set defining the cylinder in the third IB simulation*

## 6.2 - Flow past an impulsive started cylinder

This test case is a good benckmark to investigate the behavior of flows with moving bodies. Furthermore, an analytical solution exists in literature ([37]) for very short time and Koumoutsakos and Leonard [38] widely investigated this type of flow. Unfortunately, the available reference solutions refer to for incompressible flows and none benchmark exists for compressible flow in any Reynolds range. For these reasons, the IB results are compared with the body fitted results which are chosen as reference.

Convergence of solution have been investigated using the IB method. Simulations are carried out on three different meshes reducing the characteristic length from lc=15 to lc=5. In this case an implicit time integration method was used with CFL=20.

Furthermore, a convergence analysis in which CFL is reduced with a fixed spatial mesh is also performed. In particular three different simulations were performed also in this case with an implicit time integration method, fixing CFL=50, 20, 10 and adopting the finest mesh used in the previous convergence study, with lc=5. In all simulations the penalization factor was set to $\eta=0.01$ .

This test can be though as the reciprocal to the flow past a cylinder. In fact, if in case of the cylinder in cross flow, the body was fixed and the surrounding fluid was moving, in this case the opposite occurs: the surrounding fluid is still and the cylinder moves through the fluid with the same velocity as the fluid did in the previous test case, thus $u_{body}$=0.2357. For this reason and, as mentioned before, the fact that there are not in literature references for this case study with compressible flows, the body fitted results are used as reference. Specifically, the comparisons were performed with the finest BF simulation.

### 6.2.1 - Convergence study refining the mesh with fixed CFL

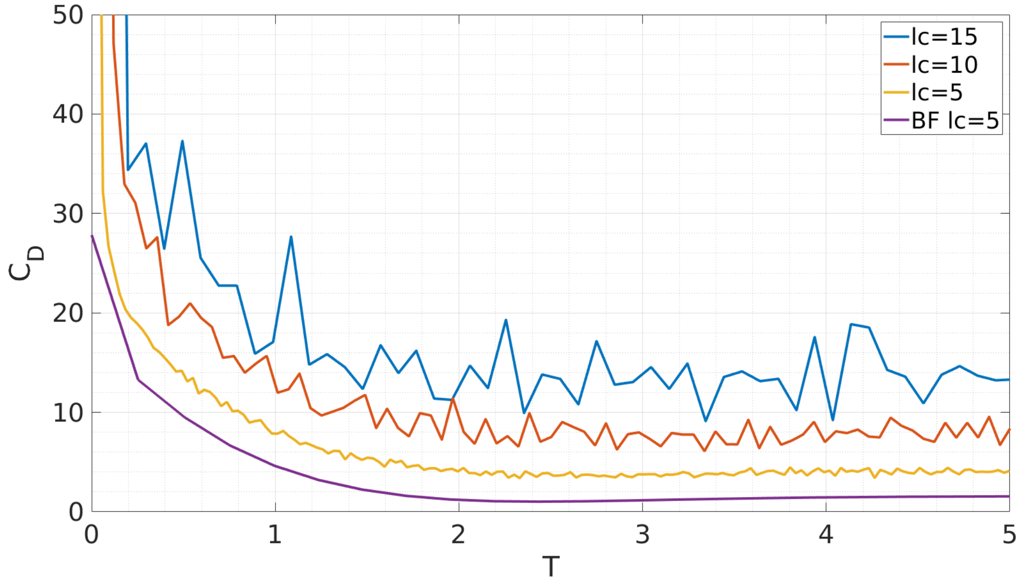


*Figure 14: Convergence of solution of an impulsive started cylinder with respect to characteristic length and time step (CFL=20)*

It can be note in Fig. 14 that as far as the characteristic length is reduced, the solution converge to the finest solution. Also a reduction of amplitude of oscillation occurs since the mesh elements size is reduced, oscillations are due to the motion of the cylinder through the mesh: the larger the mesh elements, the higher the amplitude. In fact, as said before, the cylinder is approximated in the numeric grid by the level set. If the elements have a big size, the cylinder has a non-uniform profile so the integrals of $C_D$ and $C_L$ contain numeric errors. Furthermore this non-uniform boundary changes in time as the cylinder moves, so the integral oscillates during the simulation. In this sense, if the mesh is refined, the shape of cylinder is smoother and so the integral (and $C_D$ and $C_L$ with that) is more regular.

The larger oscillations with the coarse mesh are due to the fact that, keeping fixed the CFL condition, the time-step size is related to CFL limit and the element size as $CFL=\frac{c\,\Delta t}{\Delta x}$ . In particular, if CFL is fixed, Δt is proportional to Δx. Hence, if Δx decreases, Δt decreases too. Since Δt decreases, the cylinder will do more steps in a fixed time interval (which in this case is 5 [T]) and all parameters will be calculated more times than the previous case. This leads to have more values in the fixed time interval which translates in smoother behavior.

As result of this study, we verify that the IB solution converges to the BF solution when the mesh is refined and the time step size is reduced.

### 6.2.2 - Convergence in time reducing time step size with fixed mesh

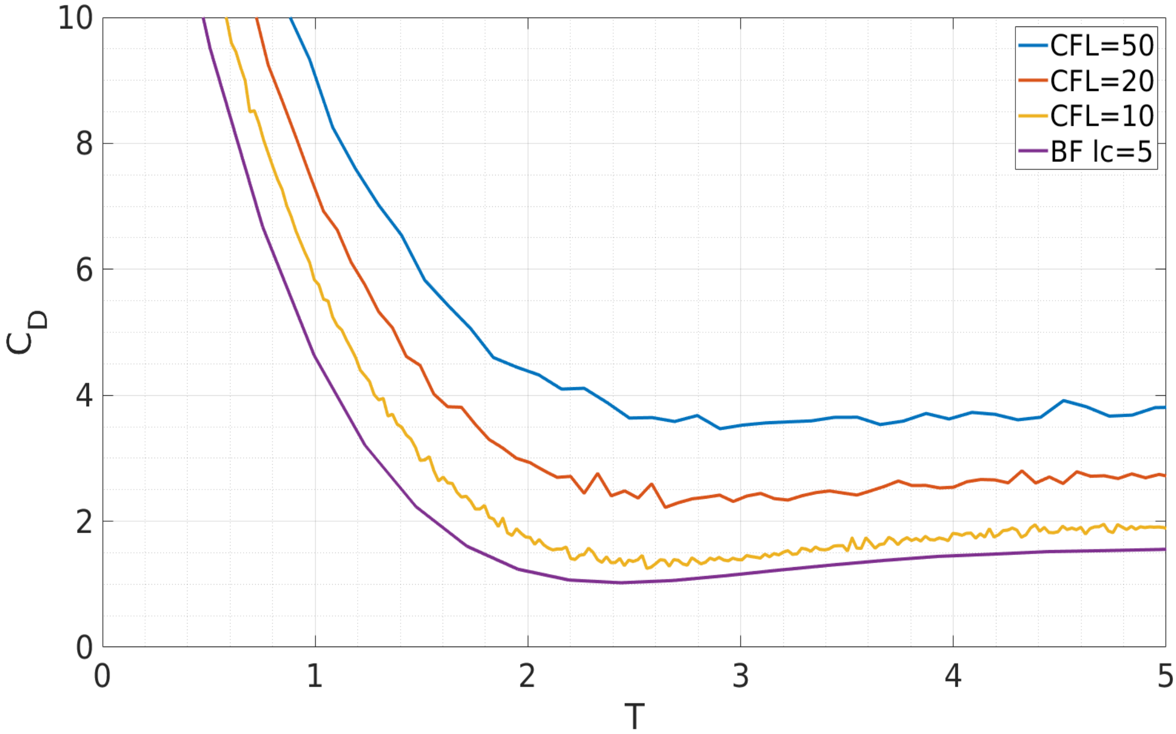


*Figure 15: Convergence of Solution of an impulsively started cylinder with respect to CFL condition (lc=5)*

As it can be noted in Fig. 15, even if Δx is fixed, Δt changes directly if CFL changes. All the effects described about amplitude and number of oscillations in Fig. 14 are still present.

Main result of this study is that as Δt decreases, the solution becomes closer to the reference one, as expected.

### 6.2.3 - $C_D$ comparison at Re=550

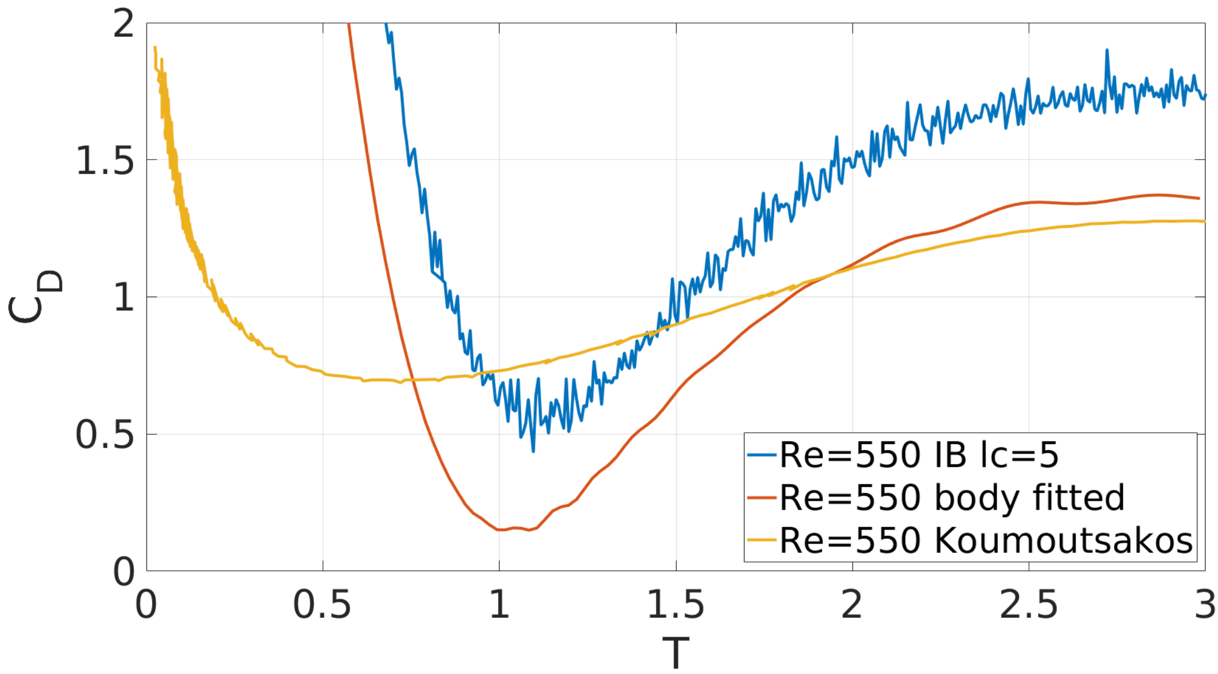


*Figure 16: Comparison between BF with fixed cylinder, IB with impulsive started cylinder and well-known solution in literature*

BF simulation was performed with an explicit time integration scheme with CFL=0.3, instead, as far as IB simulation is concerned, CFL=10 was set. Furthermore, the finest mesh of characteristic length equal to 5 was used both for BF and IB simulstions.

The available solution in the literature (in yellow) refers to incompressible flow, so the comparison, theoretically, can not be done. But, since M=0.2, an attempt can be done. Basically three features of BF and IB simulations are not in line with the reference solution: the steepest initial gradient in $C_D$ , the delay in $C_D$ drop and the minimum value reached after that.

Since a compressible flow is investigated, these differences could be simply explained. If M<0.2-0.3 and the flow is quasi-steady and isothermal, the effects of compressibility are negligible, but affect anyway the solution, as can be seen in Fig. 16. So, the effect of compressible flow are translated in a delay in drag coefficient drop, in a lower value of it reached at the beginning and a steepest gradient with whom $C_D$ drops. Since in literature there are not data of such a test case which deals with compressible flows, this result can be helpful for further and future insights.

# Chapter 7 - 2D Roots compressor simulation

## 7.1 - Assumptions

This simulation aims to test the code on a roots compressor of which physic phenomena can be well approximate in 2D since the fluid inside these type of machines moves in transverse direction without relevant phenomena occurring in axial direction. The purpose of this 2D simulation is to show the ability of the code to deal with moving boundaries.

The main idea of this test is to simulate the behavior of the code to deal with moving boundary of relative simple geometry used in compression field. Main issues are found on setting an initial and boundary condition to avoid back flow.

As first approach to this test, the physical model used to investigate the phenomena is the Navier-Stoke equations which are solved without any turbulence model while the Reynolds of the flow suggests the presence of turbulent phenomena. In fact, the Reynolds number is defined as

$$Re=\frac{\rho V_p R_p}{\mu}$$

where $\rho$ is the density of air at inlet conditions (assumed Standard conditions), $V_p$ rotor pitch velocity, $R_p$ is the rotor pitch diameter.

Working conditions are 8600 rpm as rotors speed velocity and pressure ratio equal to 1.

From profile data, male pitch diameter $R_p$ is chosen equal to 0.0423 mm. Since the male rotor speed is 8600 rpm, which is equal to 900.6 rad/s, $V_p$ =

38.1 m/s. As far as air is concerned, ρ and μ are respectively 1.16 $kg/m^3$ and 1.8 $10^{-5}$ $m^2/s$. With this data the Reynolds number is estimated approximately to be 104000.

The simulation was performed under the following assumptions:

1. the flow is characterized by subsonic regime
2. inertia and gravity effects are negligible
3. there are not other fluid inside, as cooling oil or water
4. the leakages to the outside and radial leakages are ignored during compression
5. a simplified Navier-Stokes computation is performed without a turbulence model
6. a simplified 2D simulation is performed

# 7.2 - Inlet/outlet boundary conditions approach

## 7.2.1 - Mesh and level set

Roots profiles are characterized by two or few more curves. In fact, as previously reported in Section 5.1, lobes are created starting from epicycloid and hypocycloid which are relatively simple to describe analytically. So, the level set can be easily computed. However, a different method to compute the level set is used since the final goal is to describe screw compressor geometry which is characterized by a more complex shape. The method used to calculate the level set is explained in detail in Section 8.2.1.

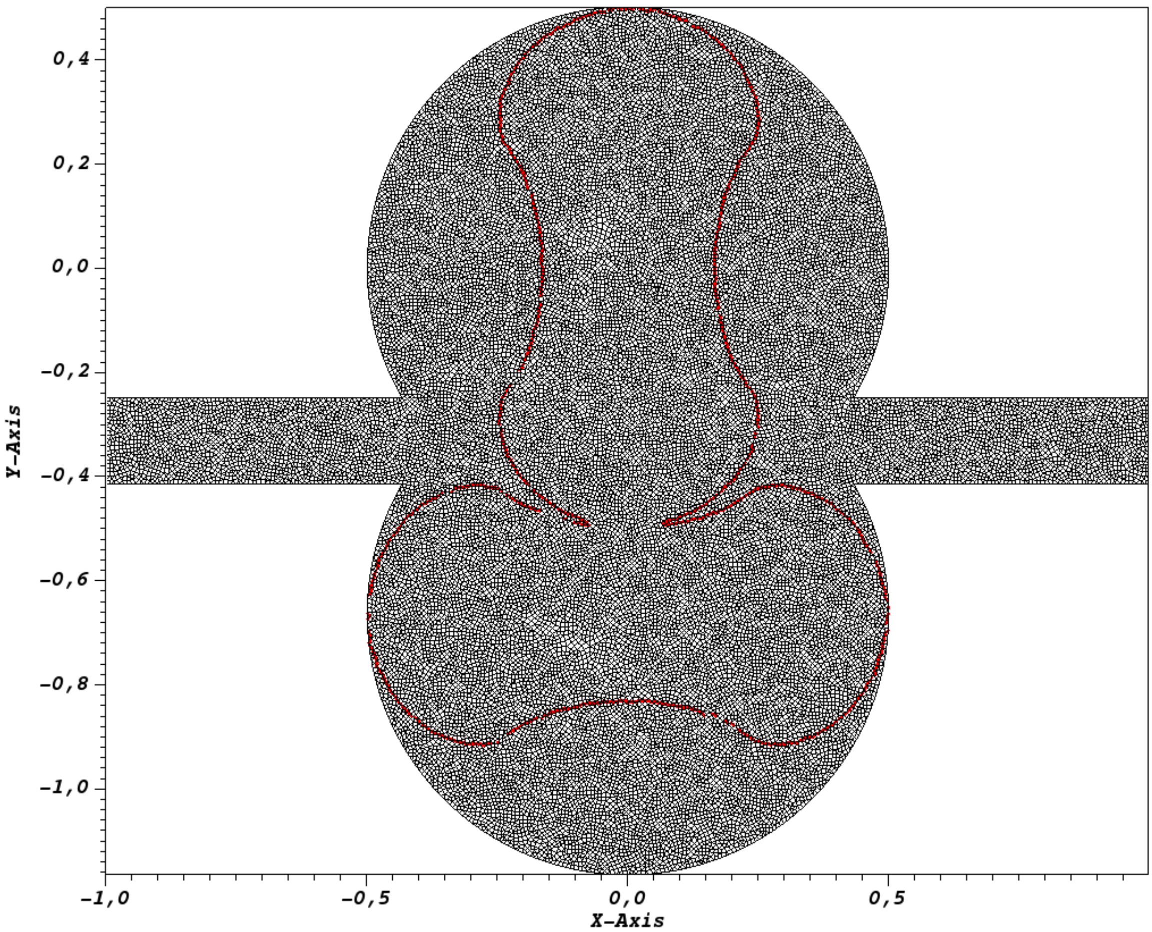


*Figure 17: Mesh of domain considered and level set which defines the roots compressor profile*

In the Fig. 17, the used mesh is presented. The penalization factor is fixed to $\eta = 5 \cdot 10^{-4}$ while the CFL=0.3 with an explicit time discretization method. The penalization factor can not be smaller since it is related to the mesh size. Smaller mesh size requires higher computational time, so a compromise is done between accuracy and computational cost.

### 7.2.2 - Boundary conditions

The proper boundary conditions must be imposed to inlet and outlet in order to reach the periodic functioning of roots compressor. In fact, main features of the internal flow can be investigated only if the initial transient flow is overcome.

Total pressure and total temperature are imposed at inlet respectively equal to 1 and 1. In fact, the code deals with adimensionalized quantity with respect to reference quantities which are listed in Tab. 7. Since the flow is supposed to go from left to right, it agrees to the reference x-direction. The inlet requires two boundary condition according to characteristic line theory in subsonic regime. Static pressure is set equal to 1 at outlet since only one boundary condition is required, as it can be seen in Fig. 18.

Domain walls are adiabatic imposing the Neumann condition and the no-slip condition is set through penalizing the momentum equation as N-S equation requires.

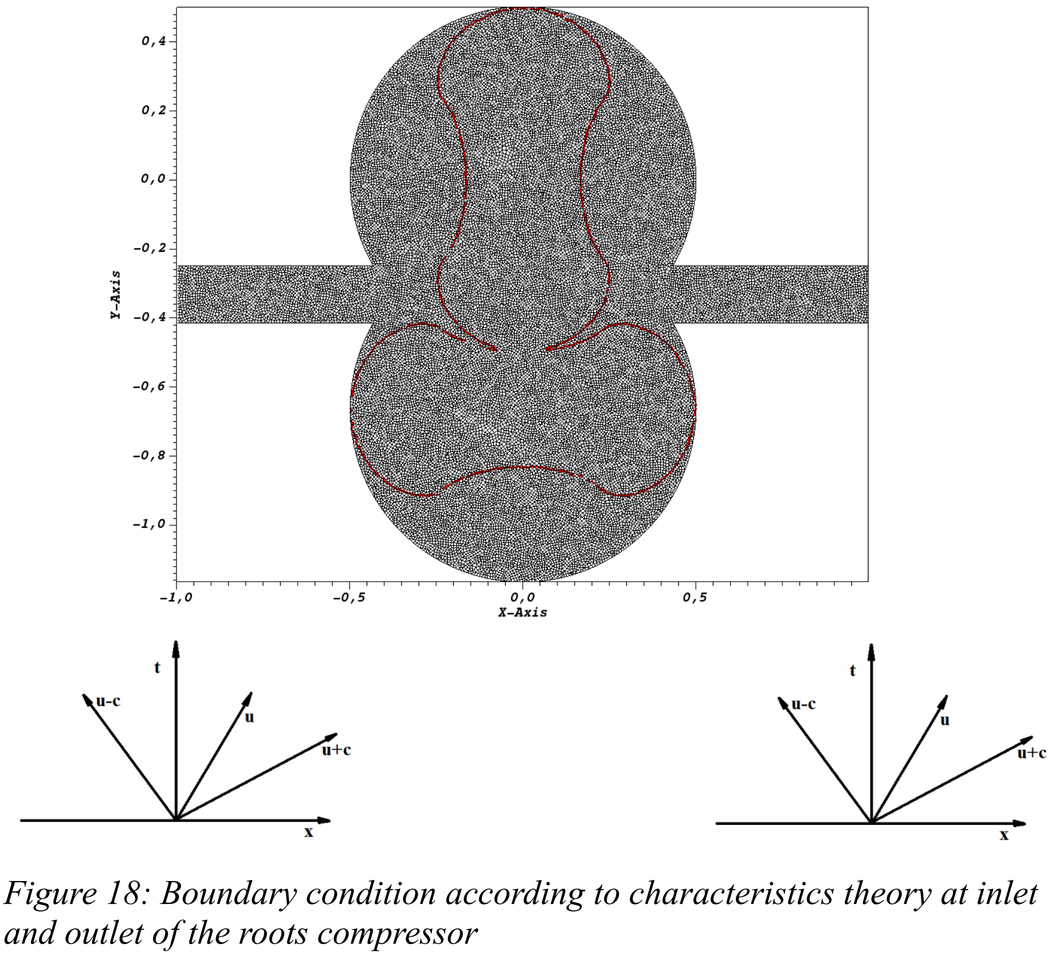


*Figure 18: Boundary condition according to characteristics theory at inlet and outlet of the roots compressor*

### 7.2.3 - Back flow problems

The used boundary conditions are not able to allow the achieving of periodic conditions. In fact, the solution is not physical when back flow verifies. Taking negative the flow entering in the system and positive the flow which exits from the control volume, it can be seen in Fig. 19 that back flow occurs at T=10.6.

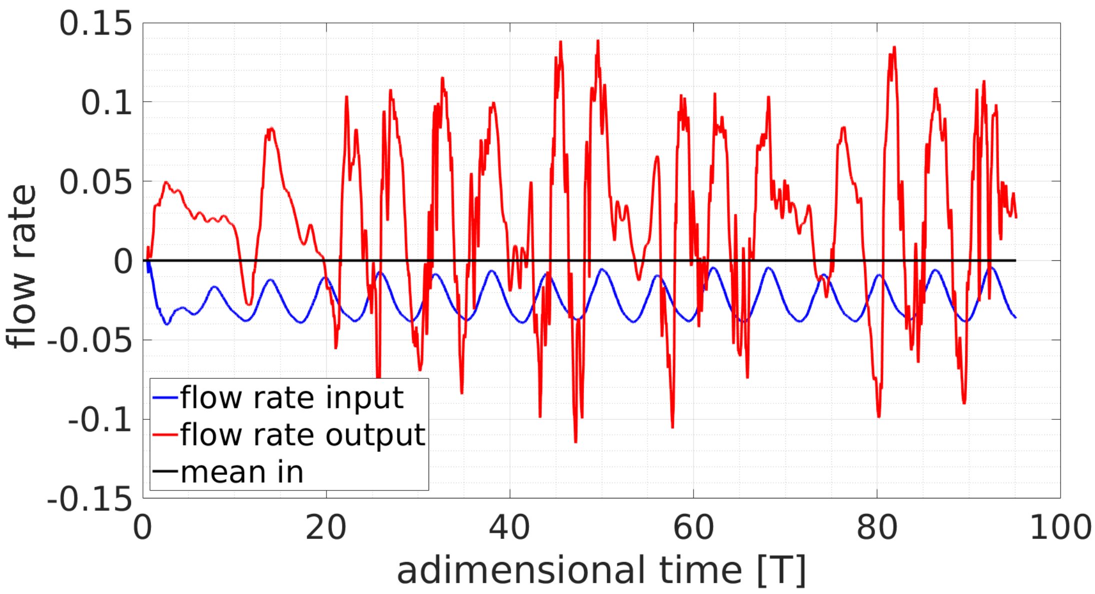


*Figure 19: Roots compressor flow rate plot at inlet and outlet of domain*

Since the flow at outlet is inverted, the velocity is opposite to the reference direction, so the solution of the Riemann problem changes according to Fig. 20.

Two boundary condition now are required to the outlet while the code imposes one condition, so the solution is no more physical.

Among the various strategies which could be adopted in order to avoid back flow, inlet and outlet boundaries are substituted by two tank large enough to allow the flow to reach periodic conditions, as described in the following.

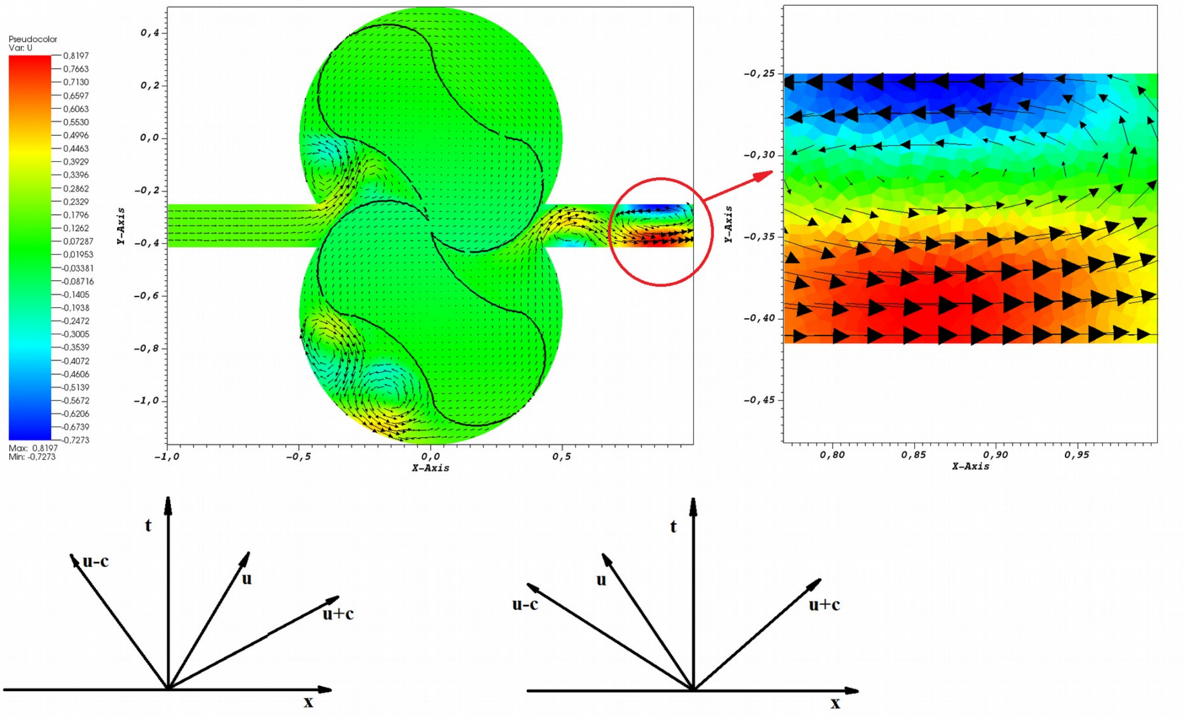


*Figure 20: Back flow occurring at inlet at T=10.6. Zoom on outlet of roots compressor. New solution of Riemann problem. Pseudocolor legend describes the x-component of velocity.*

## 7.3 - Two tanks simulations

Since back flow occurs when boundary condition in Section 7.2.2 are applied, a different approach in order to reach periodic condition is adopted. The idea is simulate roots compressor between two tanks at adimensionalized pressure equal to 1 in order to move fluid from one tank to another. In fact, in this way the domain has not any inlet or outlet.

### 7.3.1 - Mesh

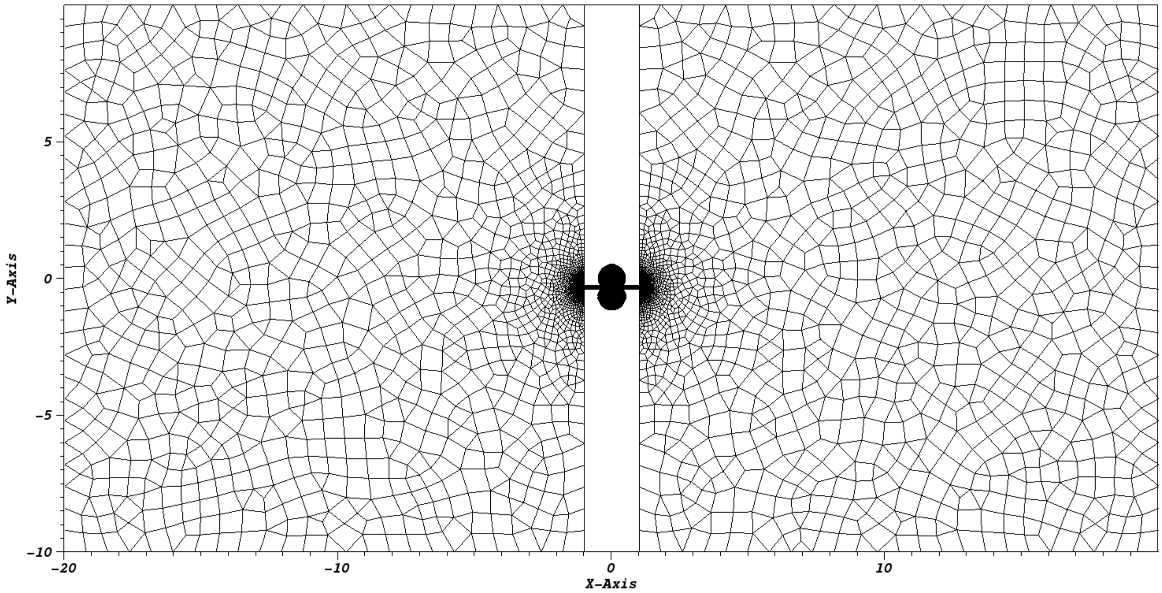


*Figure 21: Numerical grid with two tanks and roots compresor in the middle*

This time, a finer mesh was used and so $\eta=5\cdot10^{-4}$ was set as penalized coefficient. Also in this case, a CFL=0.3 was used.

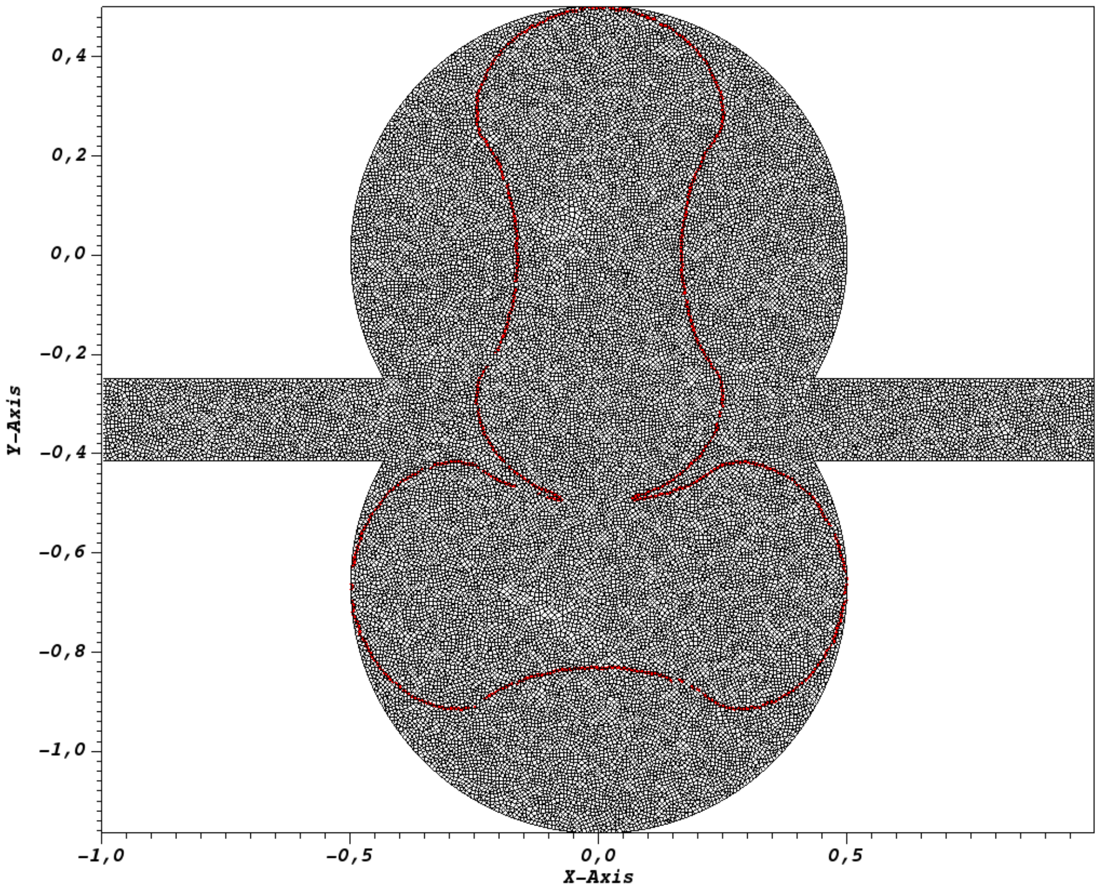


*Figure 22: Zoom on roots compressor*

### 7.3.2 - Two tanks simulation

Inlet and outlet mass flow rate at interface $x=\pm 1$ are computed each time step since periodicity is reached. Power absorbed by roots compressor is computed starting from the forces acting on the rotors. It is calculated as

$$\int_{\Omega_{male}} F \cdot \bar{u}\, d\,\Omega_m + \int_{\Omega_{female}} F \cdot \bar{u}\, d\,\Omega_f$$

where $\bar{u}$ is the velocity vector inside the solid. These integrals correspond also to the integral of the source term of the energy equation.

Remembering the reference for mass flow rate taken positive if it leaves the control volume (Fig. 22) and negative if it enters in the roots compressor, results are summarized in Fig. 23.

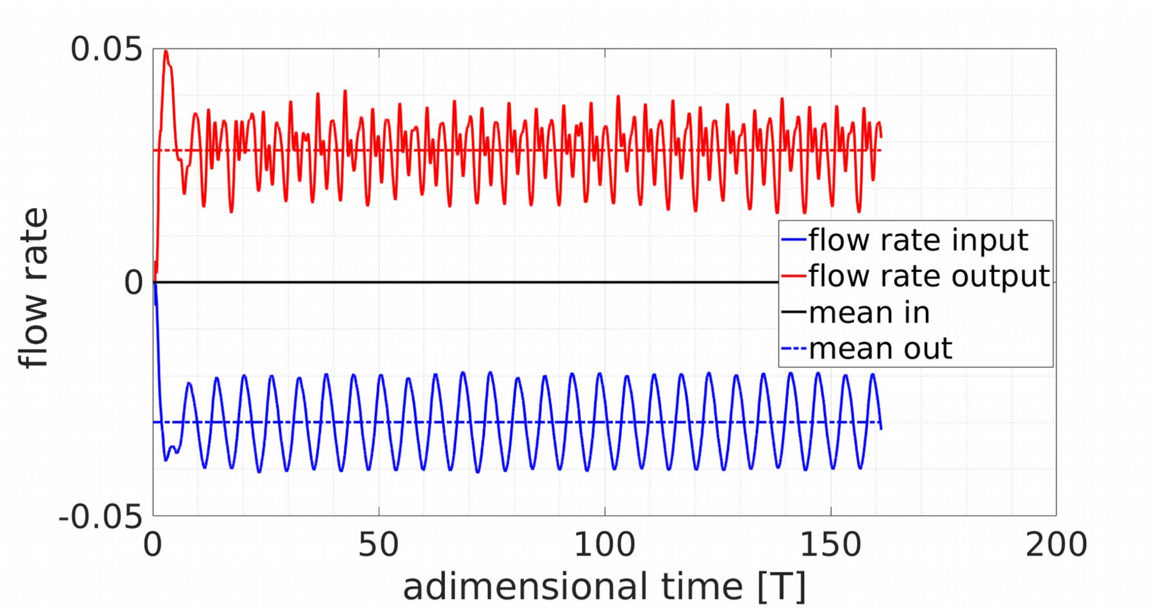


*Figure 23: Input and output mass flow rate of roots compressor between two tanks at pressure equal to 1 and rotational speed of 8600 rpm*

It can be noted that after about T=30 the solution becomes periodic. Adimensional values for inlet and outlet mean flow rate are respectively 0.0299 and 0.0282. An error of 5.5% is present in outlet mean flow rate with respect the mean inlet flow rate. That suggests that even if periodicity seems to be reached, somewhere inside the control volume of roots compressor there is a sink of mass which absorbs the missing flow rate at the outlet.

After further investigation it is found that, as it can be seen in Fig. 24 and Fig. 25 , the density of rotors is increasing. Specifically, rotor density is increasing at the interface where pressure increases. Pressure acts like the driving force both to pump the fluid in the outlet tank and to push some fluid inside the rotors. Since the density is increasing in the rotors, it can be asserted that rotors absorb mass and do not release it, so act like a mass sink.

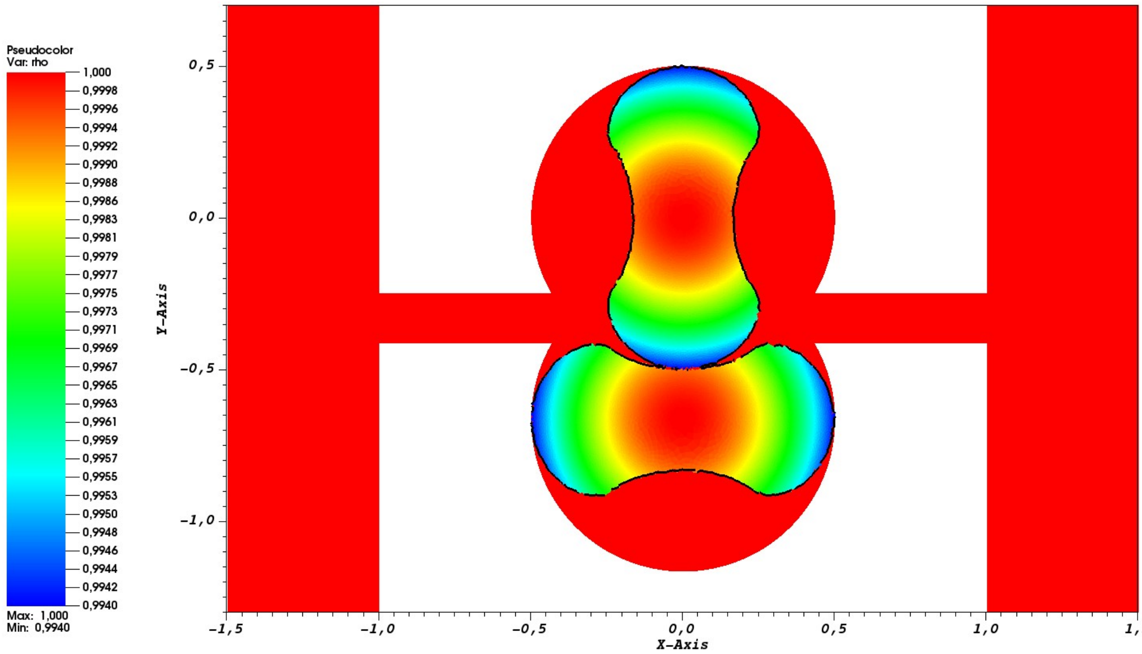


*Figure 24: Density of roots rotors at T=0*

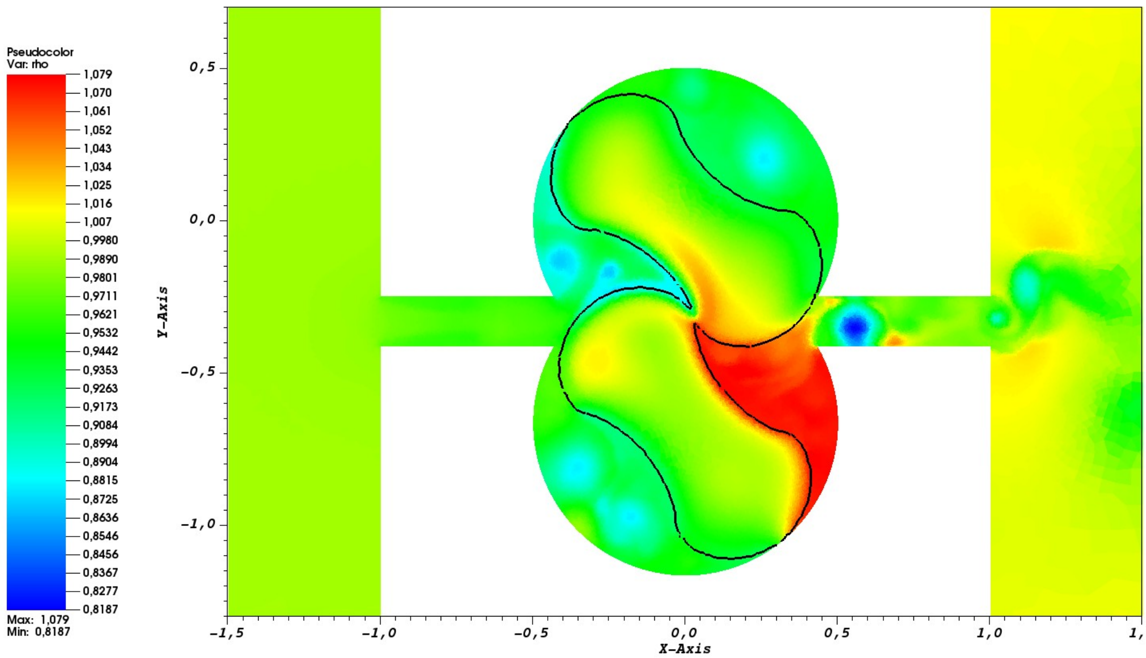


*Figure 25: Density of roots rotors at T=160*

This phenomena can be explained taking into account two main error carriers. The first contribution to the error is related to the presence of moving solid boundaries. In fact, as the solid moves through the mesh elements, a numeric error is present in results due to the approximated integrals computed at the solid boundary. Since the rotors keep moving through the mesh, the error shows some cumulative effects. This phenomena is seen also in the test case regarding the impulsive started cylinder manifesting as the amplitude oscillations in the solution of $C_D$. The solution will be more similar to the BF simulation results and the amplitude of oscillations lower as the mesh is refined, but oscillation in solution remain.

The second contribution is related to the numeric method used. In fact, the main idea of the penalization method is consider the solid as porous medium. The lower the penalization factor $\eta$ the lower the porosity of the solid bodies. So, as porous bodies, the rotors can absorb mass from surrounding. This sink effect reduces as $\eta$ decreases. A further consideration regarding the penalization method is that penalization is applied only to momentum and energy equation.

# Chapter 8 - 2D Screw compressor simulation

## 8.1 - Assumptions

After the validation of the method in the cylinder flow, a preliminary study of flow in a screw compressor is performed. The flow in a screw compressor is characterized by 3D phenomena because the moving rotors force the fluid to move in the axial direction.

The preliminary 2D simulations performed in this work represent a proof-of-concept: their purpose is to show the ability of the numerical method to deal with moving complex geometry. However, the 2D simulations cannot describe the axial displacement of the fluid trapped in the cavity defined by the two rotors. For this reason, the simulations presented in the following represent just a first numerical step to discover some problems related to this flow (for example the definition of proper initial and boundary conditions to avoid reverse flow). Also the physical model is simplified: the Navier-Stoke equations are solved without any turbulence model while the Reynolds of the flow suggests the presence of turbulent phenomena.

This preliminary study represents a first step towards more detailed future 3D studies.

Assumption made in this case are the same of the roots compressor test case, which are listed below for more clarity.

1. the flow is characterized by subsonic regime
2. inertia and gravity effects are negligible
3. there are not other fluid inside, as cooling oil or water

4. the leakages to the outside and radial leakages are ignored during compression
5. a simplified Navier-Stokes computation is performed without a turbolence model
6. a simplified 2D simulation is performed

First of all, the main concern results in Reynolds number definition. As reported by Guerrato [39], the Reynolds number for screw compressor is defined as

$$Re = \frac{\rho V_p R_p}{\mu}$$

where $\rho$ is the density of air at inlet conditions (assumed Standard conditions), $V_p$ is the male rotor pitch velocity, $R_p$ is the male pitch diameter.

In order to have a comparison as closest to reality as possible with data in literature [40], a male rotor speed of 8600 rpm is chosen. A screw compressor profile with 5/6 lobes was used with compression ratio equal to 2, since the purpose of this test is to simulate an industrial application of it.

From profile data, male pitch diameter $R_p$ is equal to 56.65 mm. Since the male rotor speed is 8600 rpm, which is equal to 900.6 rad/s, $V_p$ = 50.9 m/s. As far as air is concerned, ρ and μ are respectively 1.16 kg/m$^3$ and 1.8 10$^{-5}$ m$^2$/s. With this data the Reynolds number is estimated approximately to 185000.

# 8.2 - Inlet/outlet boundary conditions

## 8.2.1 - Mesh and level set

The screw compressor geometry is adimensionalized using as reference length $A_c$ which, as reported in Section 5, is the distance between the two rotors.

Since the shape of the profile is complex, a simple analytic level set, such as in case of a circular cylinder, is no more usable. So, a level set is computed numerically by discretizing the body with a finite number of points. The computation is based on the signed external product. First of all, the distances between the generic mesh point and all the points which describe the solid boundary are computed and the minimum is identified and so the point of the boundary (S) nearest to the mesh point is considered (P). Profile points are defined in counter clock-wise. After that, two vector are defined: the ‘profile vector’ and ‘distance vector’. The fist is given by the vector which goes from the preceding point of profile (R) to the point S, which is the nearest to the mesh point P. and the vector which goes from the mesh point considered (P) to the nearest one of the compressor profile (S) . In this way two vectors are properly defined. Now, defining the external product as

$$\boldsymbol{c}=\boldsymbol{a}\times\boldsymbol{b} \quad .$$

The sign of the z-component will define if it is an internal or external point. In particular, if it is negative, as in case of $\boldsymbol{c}=\boldsymbol{a}\times\boldsymbol{b}'$ , the point will be inside the solid boundary. If it is not, it is an external point. Then, the minimum signed distance of the mesh point is allocated in order to reconstruct the compressor profile which results the locus of mesh points which has distance equal to zero. The internal points are given by those points whose have negative distance and external points are defined by a positive distance. A simple scheme is shown below:

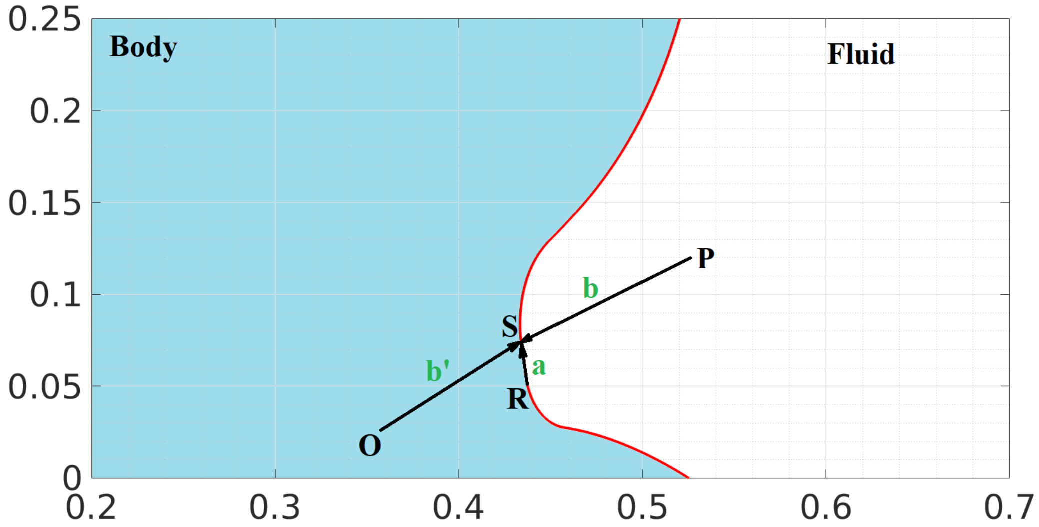


*Figure 26: Schematic representation of the internal product to define the sign of the distance calculated by the level set*

the only requirement of this approach is that a sufficiently fine sampling of the level set is performed: in this work the distance between two consecutive profile points is chosen as $10^{-5}$.

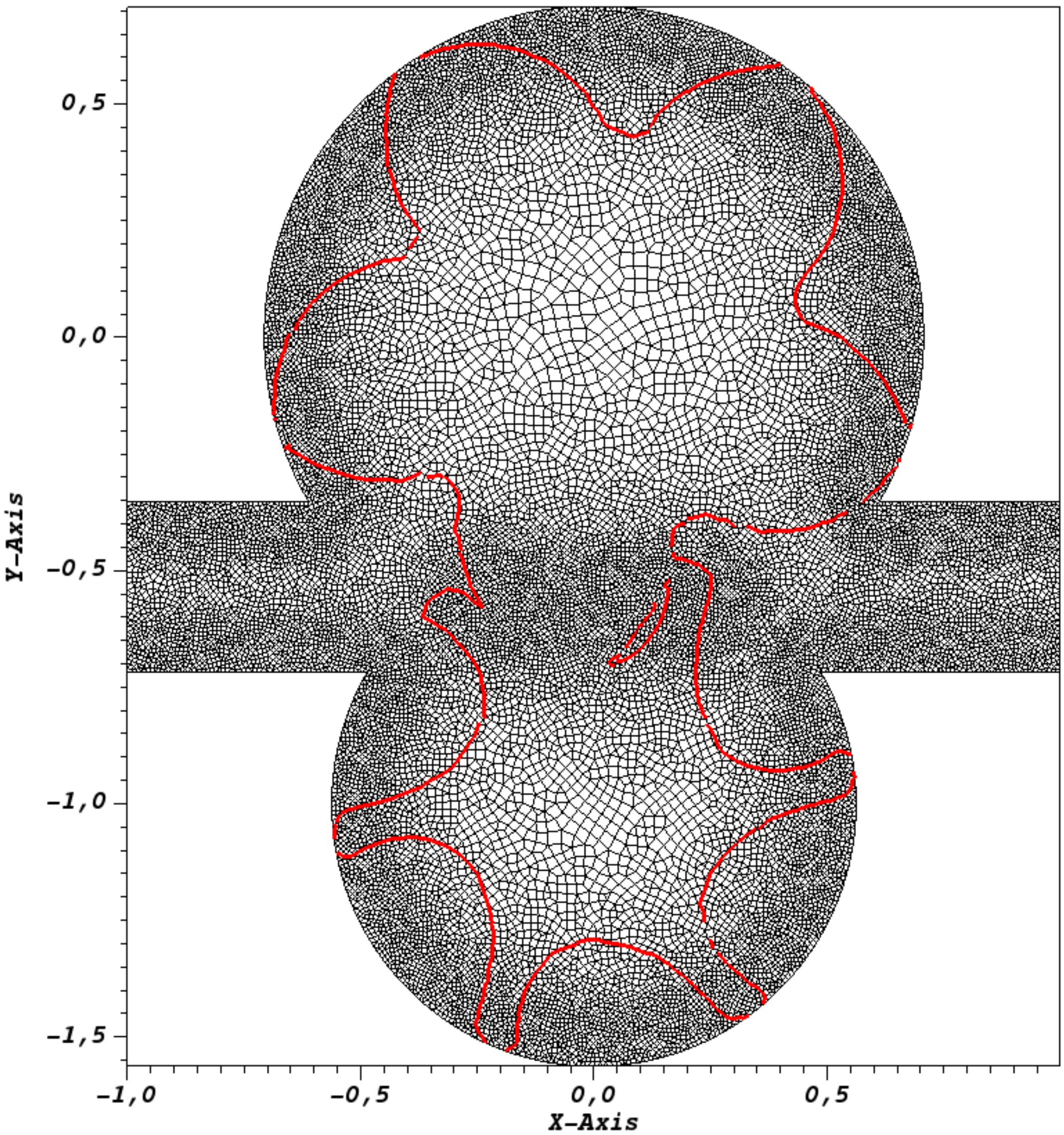


*Figure 27: Mesh of domain considered and level set which defines the screw compressor profile*

In the Fig. 27, the used mesh is presented. The penalization factor is fixed to $\eta=5\cdot10^{-4}$ while the CFL=0.3 with an explicit time discretization method.

*Table 7: Adimensionalized quantities*

| **Adimensionalized quantity** | **Formula** | **Value** |
|---|---|---|
| $p_{ref}$ | - | $10^5$ Pa |
| $L_{ref}$ | - | 80 mm |
| $T_{ref}$ | - | 300 K |
| $\rho_{ref}$ | - | 1.16 kg/m$^3$ |
| $\mu_{ref}$ | - | 1.8 $10^{-5}$ m$^2$/s |
| R | - | 287 J/kg/K |
| $u_{ref}$ | $\sqrt{(RT_{ref})}$ | 293.4 m/s |
| $t_{ref}$ | $\frac{L_{ref}}{u_{ref}}$ | 2.17 $10^{-4}$ s |
| $\omega_{ref}$ | $\frac{1}{t_{ref}}$ | 3663 rad/s |

### 8.2.2 - Boundary conditions

It is acknowledged that periodic conditions are not reached in case of roots compressor test imposing inlet-outlet boundary conditions but, since a new test with different working conditions is investigated, they represent the natural set of BCs if periodic state would be achieved.

Results obtained will be used to make mass flow rate comparison with results in literature, specifically with results in [40]. As far as inlet is concerned, total pressure and total temperature are imposed respectively equal to 1 and 1 (since is adimensionalized temperature). Two boundary conditions are required because of the solution of Riemann problem applied on inlet boundary. The fluid goes from left to right and, according to reference, the fluid velocity is positive. So, the solution of Riemann problem is outlined in Fig. 28 according to subsonic regime assumption. Since two characteristics are entering in domain, two boundary conditions are required in order not to violate the physics.

Instead, considering the Riemann solution at outlet, only one boundary condition is required since only a characteristic line is entering in domain. So, the static pressure outlet is imposed to change as a ramp from 1 to 2 in two rotations of male compressor, so

$$p(t)=\begin{cases} 1 & t<\frac{\pi}{\omega} \\ 1+1\cdot\frac{\left(t-\frac{\pi}{\omega}\right)}{\frac{\pi}{\omega}} & \frac{\pi}{\omega}\geq t>\frac{2\pi}{\omega} \\ 2 & t\geq\frac{2\pi}{\omega} \end{cases}$$

where $p$, $\omega$, $t$ are adimensionalized quantity with respect reference quantities in Table 7.

Each wall was set to be adiabatic with the Neumann condition and the no-slip condition is imposed to the momentum equation near the solid boundary, as required by use of N-S equations.

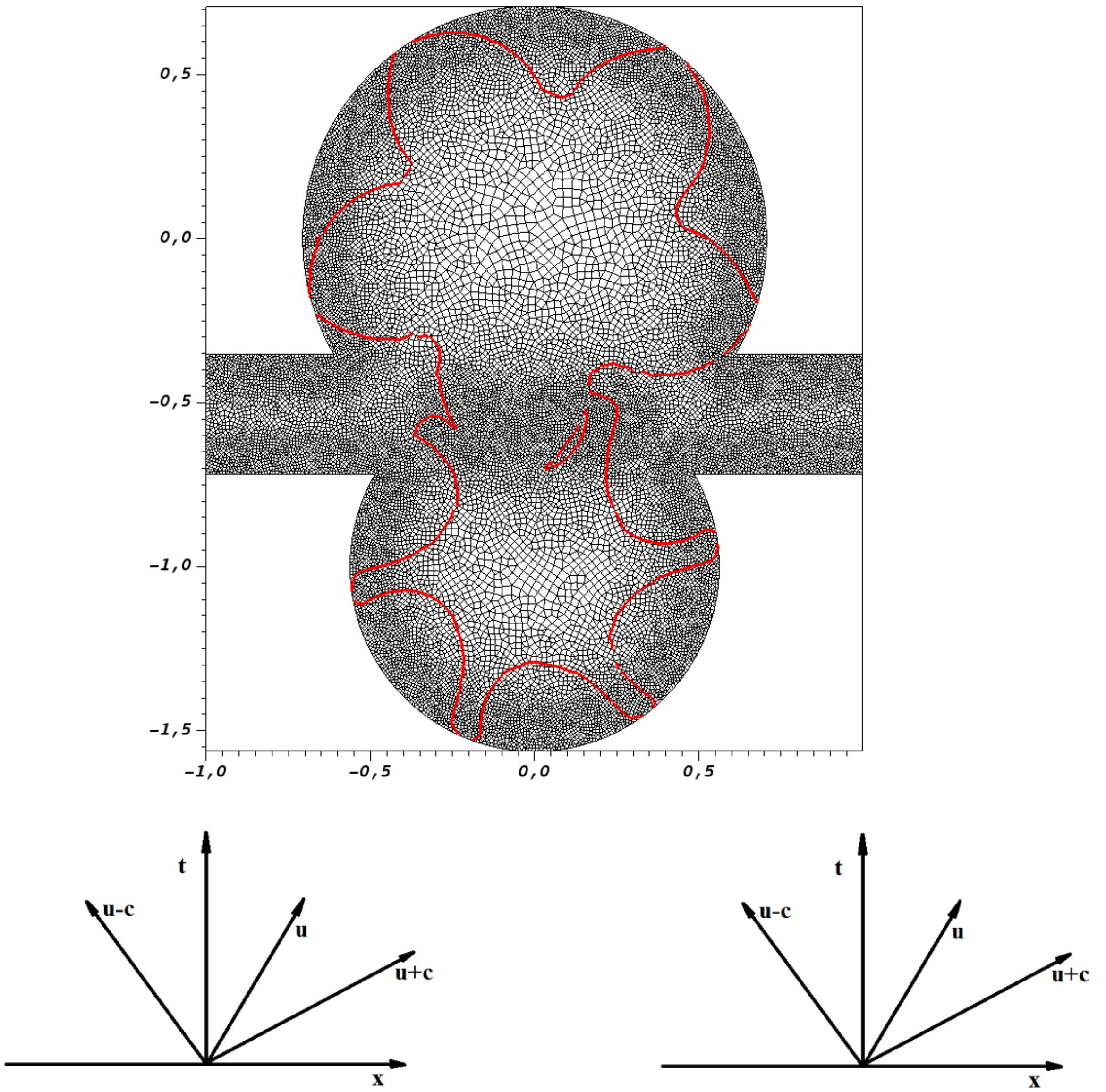


*Figure 28: Boundary conditions according to Characteristic theory at inlet and outlet of the screw compressor*

### 8.2.3 - Back flow problems

Unfortunately, this boundary condition is not able to make the simulation reach a periodic condition. In fact a back flow occurrence can verify, as in roots compressor case. So, the solution is no more physical. Inlet flow entering in domain is taken negative and outlet flow which goes out from domain is taken negative. With this agreement, the occurrence of back flow verifies at T=0.61 as it can be seen in Fig.29.

In this condition, the fluid velocity is negative since the flow goes locally from right to left. So, the velocity is negative and the solution of Riemann problem, should change according to Fig.30.

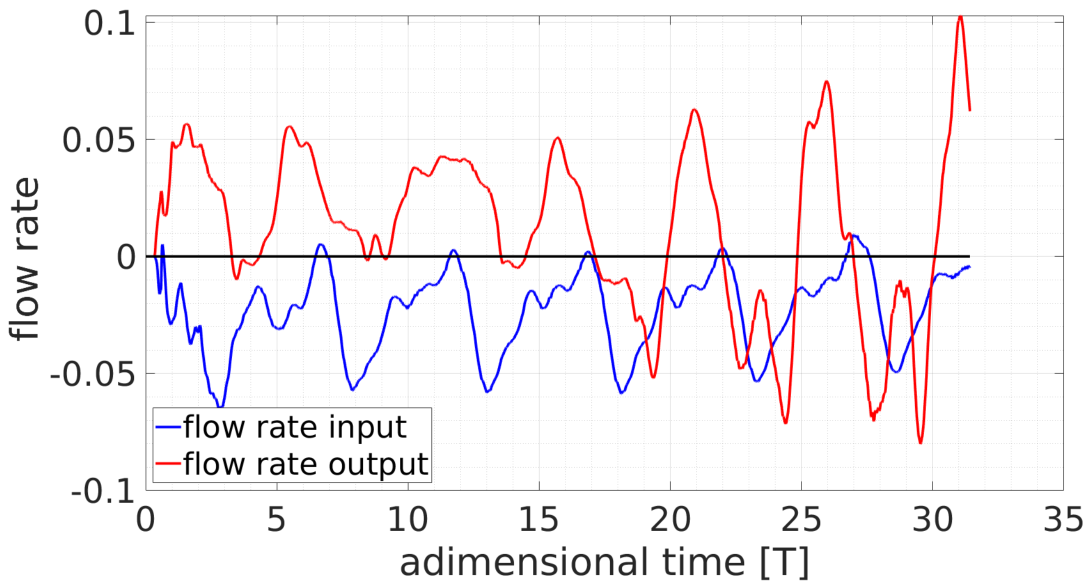


*Figure 29: Flow rate plot at inlet and outlet of the screw compressor*

Only one boundary condition is now required at inlet while the code imposes two conditions at inlet and so the results can not be considered physical.

An attempt of decreasing the gradient of the pressure ramp was made doubling the delay of pressure rising. Unfortunately, the same result comes out. The easiest way to solve back flow problem, avoiding non-physical results, is the same approach used in roots compressor simulation. So, screw compressor is located between two tanks at different static pressure, as described in next sections.

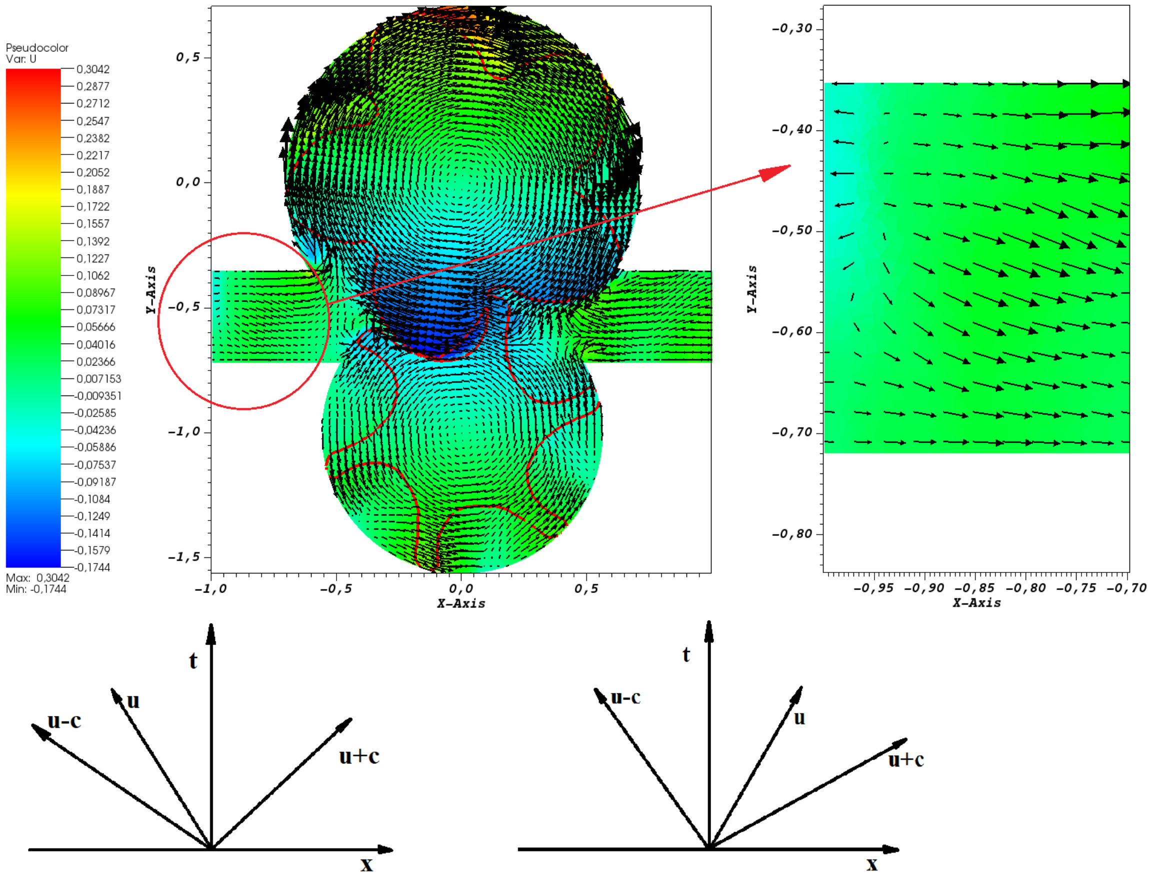

*Figure 30: Back flow occurring at inlet at T=0.61. Zoom on inlet of the screw compressor and solution of Riemann problem. Pseudocolor legend describes the x-component of the velocity vector.*

## 8.3 - Two tanks simulations

As mentioned before, the first tested approach in order to reach the periodic conditions can give problems due to back flow, so a different method was investigated. The idea behind the following approach, as previously said in roots compressor test case, is to simulate the compressor between two large pressurized tanks. In this way the computational domain does not contain any inlet or outlet. The aim is transport air from the low pressure tank to high pressure tank. The pressure on the left tank was set to 1, instead, the pressure on the right tank was imposed equal to 2, according to non-dimensionalization of parameters.

### 8.3.1 - Mesh

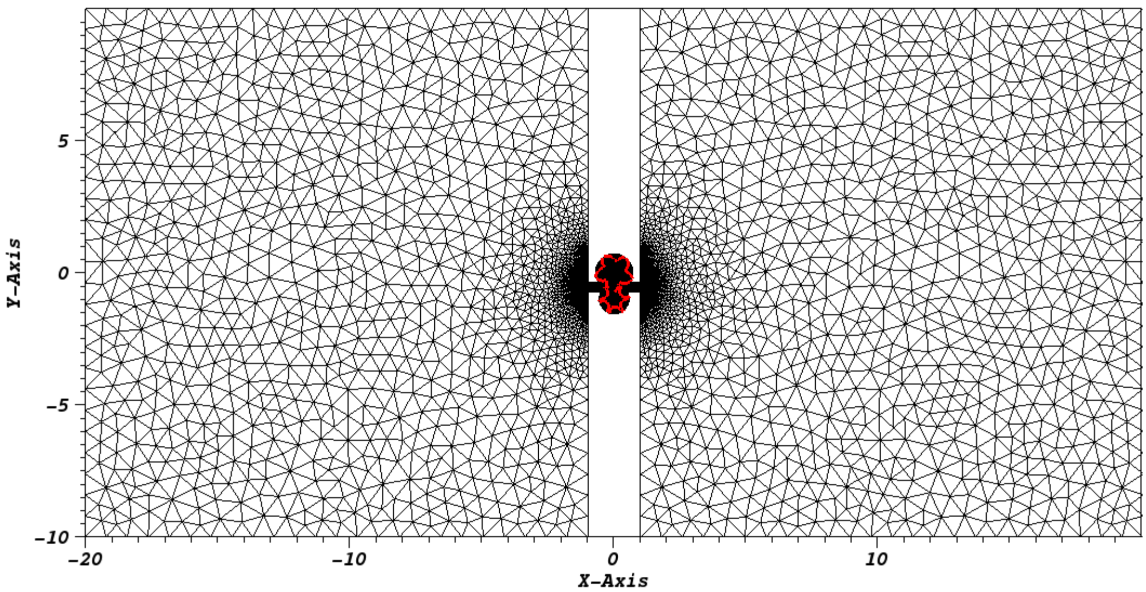


*Figure 16: Numerical grid with two tanks and screw compressor in the middle*

This time, a finer mesh was used and so $\eta = 5 \cdot 10^{-4}$ was set as penalized coefficient. Also in this case, a CFL=0.3 was used.

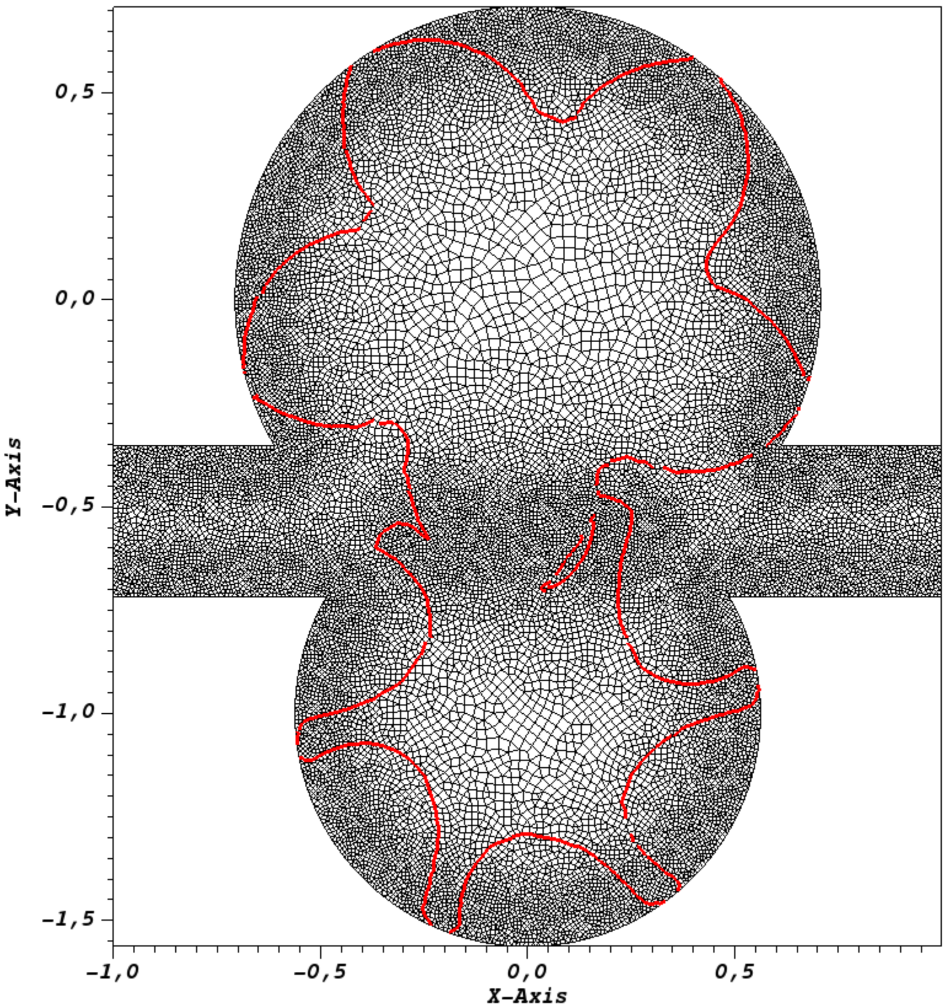


*Figure 17: Zoom on screw compressor*

### 8.3.2 - Results

Each time step the flow rate at inlet and outlet and the power absorbed by the screw compressor are computed. Specifically, inlet and outlet mass flow rate are computed at $x=\pm 1$ interfaces. The power is calculated starting from the forces acting on rotors. It is calculated as

$$\int_{\Omega_{male}} F\cdot\bar{u}\, d\,\Omega_m + \int_{\Omega_{female}} F\cdot\bar{u}\, d\,\Omega_f$$

where $\bar{u}$ is the velocity vector inside the solid. These integrals correspond also to the integral of the source term of the energy equation.

Since the comparison was made between screw compressor with 3/5 and 5/6 lobes and the same speed of 8600 rpm, is expected that in the time required for a full rotation respectively 3 and 5 oscillations in flow rate occur. The flow rates at inlet and outlet are also different since, excluding the fact that the comparison was done with a computed flow rate involving a 3D screw compressor model, there are more lobes in rotors and the space available for air is reduced and so the flow rate which can be provided is lower.

Remembering that the inlet flow rate is negative when it enters in the control volume of the screw compressor and the outlet flow rate is positive when it leaves the control volume, results obtained are summarized in Fig.31 and Fig. 32.

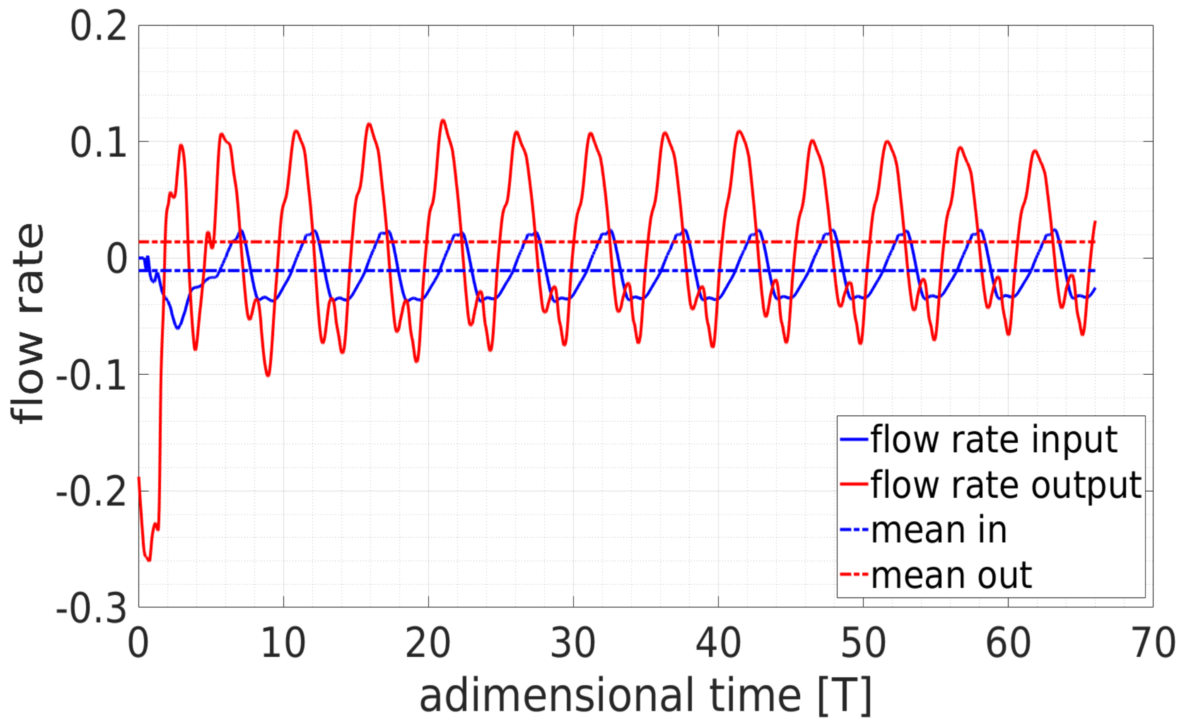


*Figure 31: Input and output mass flow rate of screw compressor between pressurized tank with rotational speed of 8600 rpm and pressure ratio equal to 2*

It can be noted that initially the output flow is totally negative. This is due to the fact that the pressure inside the compressor was initialized equal to 1 until $x=1$. So a huge back-flow occurs immediately at outlet. The oscillations almost stabilize after T=30 but their amplitude is still decreasing and it will continue until the whole air contained in tank 1 is transported in tank 2, when the mass flow rates oscillation decrease to 0, but, since the tanks are larger, an interval in which the flow rate is stable is expected.

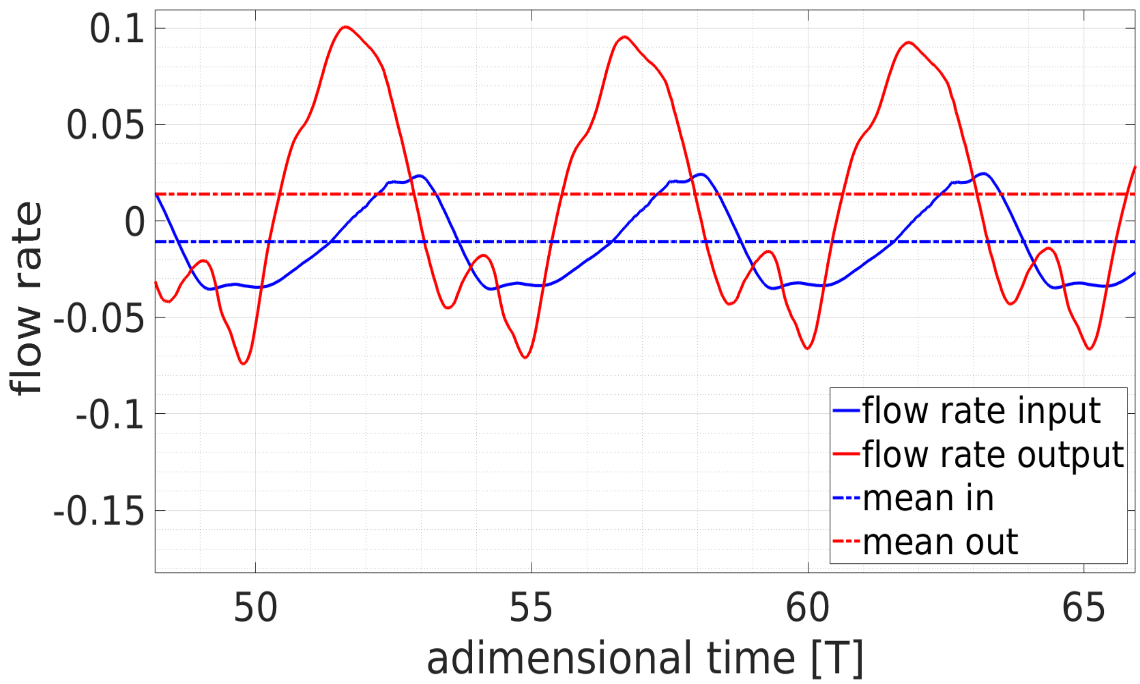


*Figure 32: Zoom on flow oscillations when periodicity is almost reached*

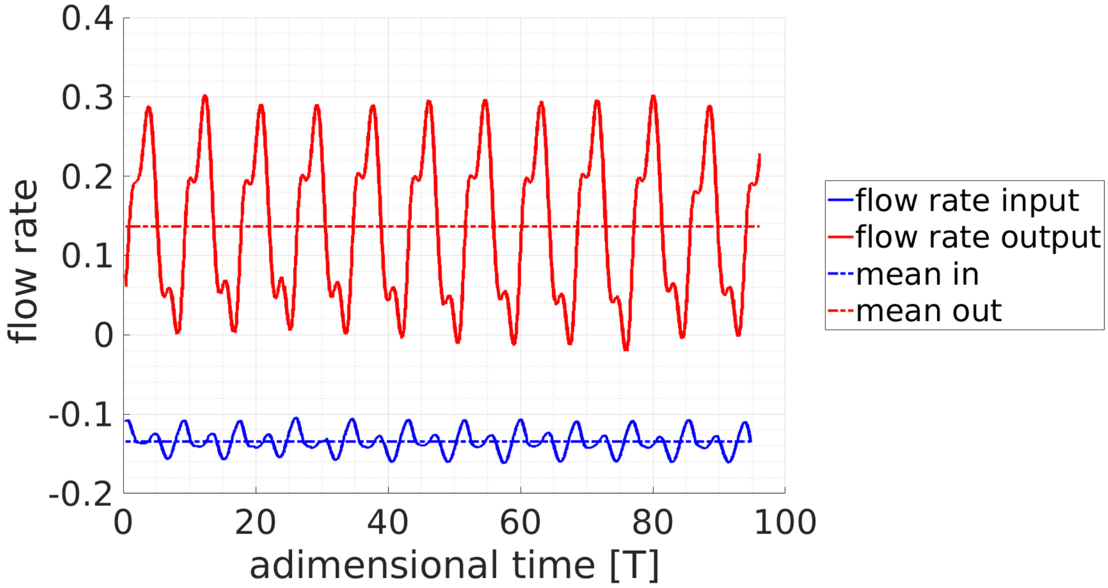


*Figure 33: Reference mass flow trend in 3/5 screw compressor with male rotor speed of 8600 rpm and pressure ratio equal to 2 [40]*

Comparing 2D simulation results in Fig. 32 with the reference in Fig. 33, it can be noted that the mass flow rate trend computed with the 2D simulation is similar to the one computed with a 3D model. The mean mass flow rate in input and output of the reference are respectively 0.134 and 0.137 kg/s.

However, the inflow and outflow mean mass rates are not equal like Fig. 32 suggests. In fact, the inlet and outlet adimensional flow rates of the last 5 periods are respectively 0.0105 and 0.0139.

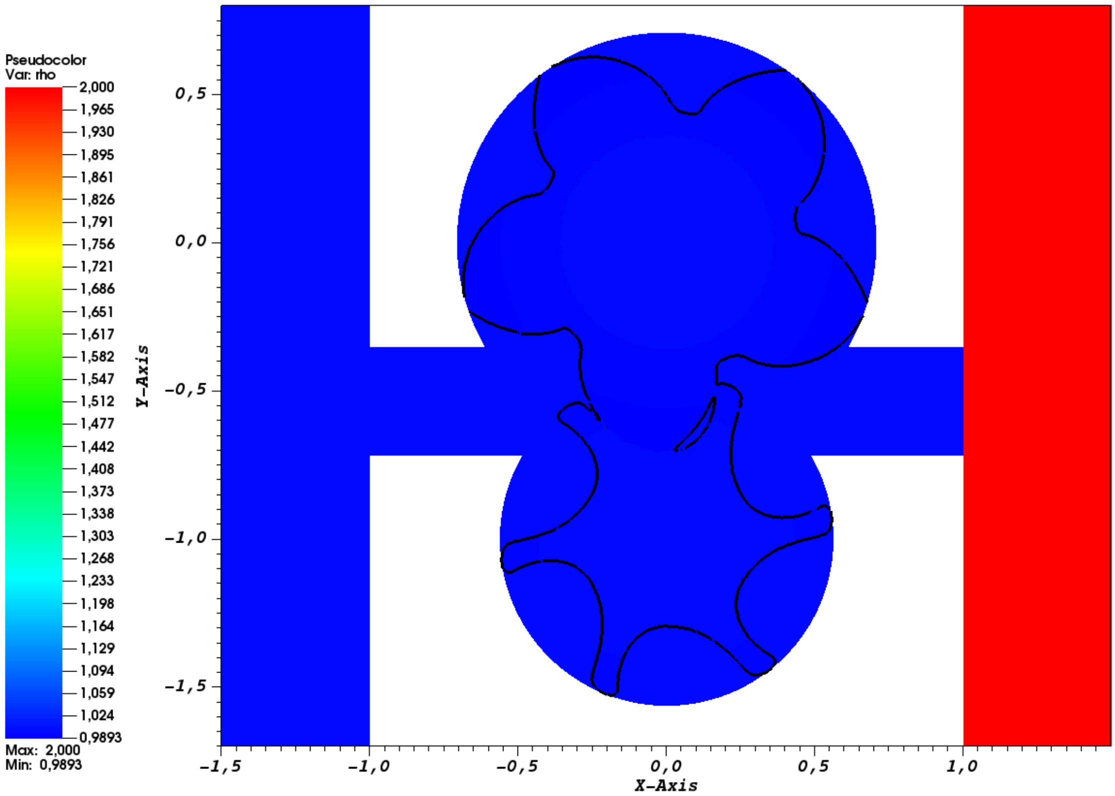


*Figure 34: Density of rotors at T=0*

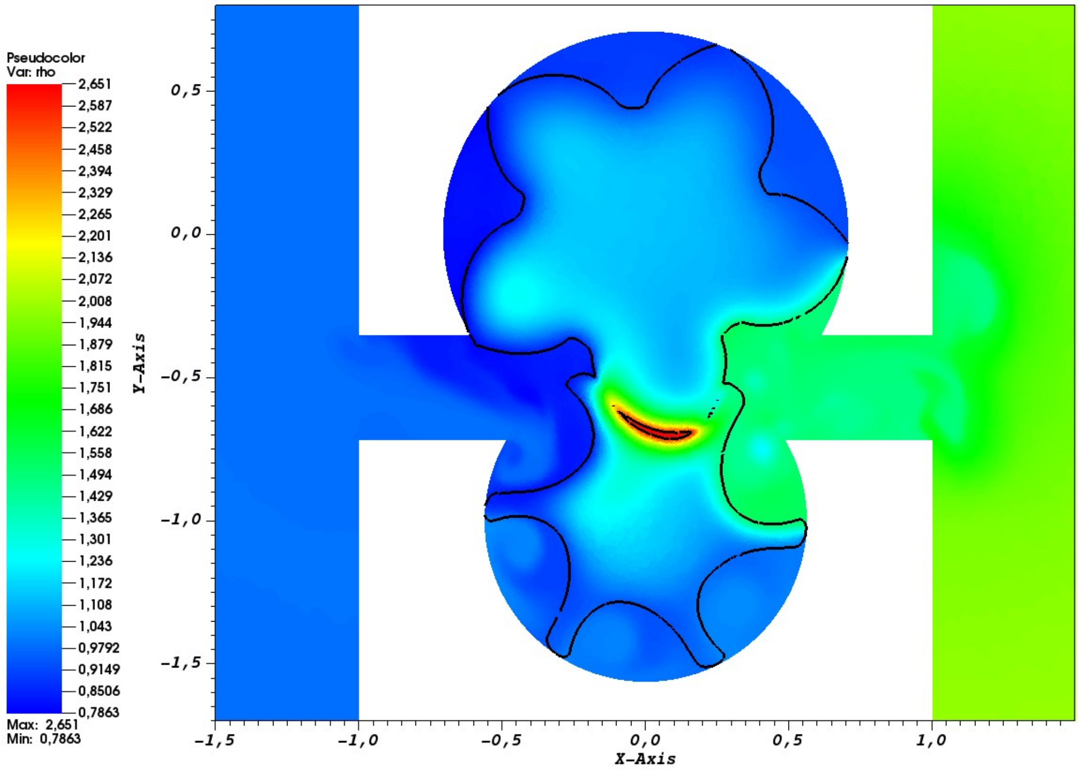


*Figure 35: Density of rotors at T=66*

This result may led to a the wrong observation that somewhere in the control volume there is a mass source, but it is not. In fact, the mean values of inlet and outlet the mass flow rate integrated from T=0 to the final time are respectively 0.0122 and 0.0076. So, as expected from results of roots compressor test, there is a mass sink and the mass conservation law is not broken. The mean flow rates of the last 5 periods are different since the periodic condition are not fully reached. In fact, it can be observed that if the roots compressor test ends at T=160, the screw compressor simulation ends earlier, at T= 66. Both simulation have been carried out with the same computational resources and the same time deadline, and, as expected, screw compressor test requires more computational time to reach the same simulation time since deals with more complex geometry which requires more number of profile points with respect to the roots lobe profiles.

Density is increasing inside the rotors as can be noted by comparing Fig. 34 with Fig. 35.

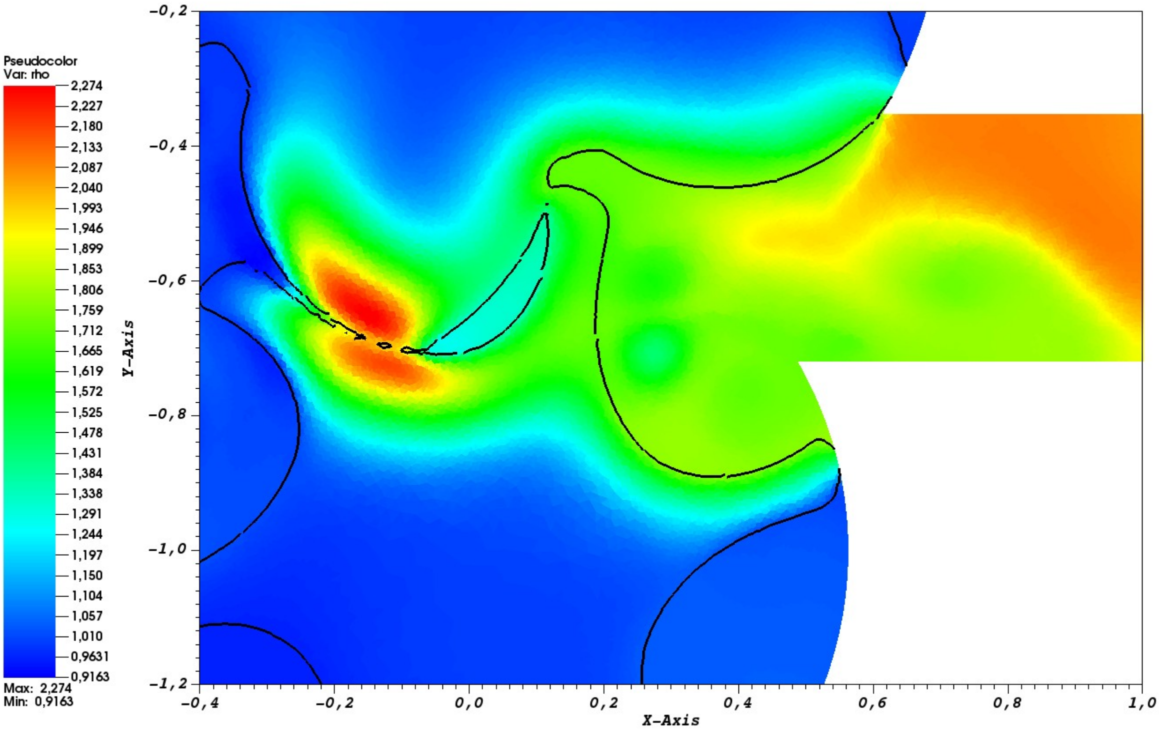


*Figure 36: Phenomenology of density increasing*

This behavior is encountered also in roots compressor simulation, but is now enhanced by higher outlet pressure and mainly by another phenomena which takes place. Tooth which match together, as it can be seen in Fig. 36, can trap air. In fact during rotation, the air gap between the two tooth reaches high pressure while progressively the gap reduces until rotors match perfectly and the gap disappears. This means that air is entering in rotors, rising up in this way its density. This phenomena is not observed in roots compressor simulation because roots lobes are always in contact and there is not formation of air gaps between them. This phenomena of air trapping which occurs is nothing but the compression in axial direction due to a volume chamber of screw compressor which disappears.

So, as far as screw compressor is concerned, the density rising in solid bodies are due to the lack of a term which penalizes density in mass conservation equation, the relative high porosity of the solid and an additional sink phenomena due to the fact that the compression process can not be fully described in 2D. All these phenomena explain why the mass flow rates are so small compared to the reference one.

The occurrence of this phenomena reflects on power calculation. In fact, since the rotors density is increasing during the process, energy storage occurs in rotors which rotate at constant speed. So, since the mass is increasing while the velocity remains constant, the kinetic energy of male and female rotors is increasing. So, the solid bodies act like a sink of mass and energy.

# Chapter 9 - Conclusions and future developments

This work represents a preliminary study to investigate the flow field in roots and screw compressors by means of penalization techniques. The results put in evidence that penalization methods work well on canonical test cases like for example the flow around a circular cylinder. However, several problems were encountered when dealing with roots and screw compressors. First of all, back flows problems were observed when inlet/outlet boundary conditions are used: a possible solution, based on the use of two large tanks, is proposed. Furthermore, some problems related to the permeability of the solid bodies were observed: in particular, the simulations show that the density inside the rotor changes in time. A possible solution could be the introduction of a particular penalization term also in the mass equation, following [41].

Finally, turbulence phenomena were not properly modelled in this preliminary work: future work should be related to the selection of valid turbulence models like for example URANS or LES approaches. Furthermore, the extension to 3D is essential for screw compressors in order to describe the axial displacement of the fluid.

# Appendix A

| **Physical model variables** | |
|---|---|
| E | Total energy (internal+kinematic) per unit volume |
| F, G | Physical fluxes |
| u | Generic conservative variable |
| $M_\infty$ | Freestream Mach number |
| p | Pressure |
| Pr | Prandtl number |
| Q | Source term in heat equation |
| $Re_{ref}$ | Reference Reynolds number obtained by adimensionalization |
| $Re_\infty$ | Freestream Reynolds number |
| S | Entropy |
| $S_{ij}$ | Mean strain rate tensor |
| T | Temperature |
| $u,v$ | Cartesian component of velocity |
| $\gamma$ | Specific heat ratio |
| $\mu$ | Dynamic viscosity |
| $\nu$ | Kinematic viscosity |
| $\lambda$ | Heat conductivity |
| $\tau_{ij}$ | Laminar stress tensor |
| $\rho$ | Fluid density |

| **Profile variables** | |
|---|---|
| $\beta$ | pitch helix angle of rotor |
| $\delta$ | distance from centre line to point A (Fig. 3) |
| $\varepsilon$ | given tollerance |

| | |
|---|---|
| $\Phi$ | rotation angle |
| $\gamma$ | included angle of circular arc EF |
| $\eta$ | upper parametric limit of trochoid CD |
| $\kappa$ | normal equidistance of trochoid CD |
| $\lambda$ | pitch lead angle of rotor |
| $\mu$ | slanted angle of ellipse FG |
| $\theta$ | curve parameter of rack |
| $\theta_1$ , $\theta_2$ | lower and upper parameter limits of ellipse FG |
| $\rho_1$ | radius of circular arc AB |
| $\rho_2$ | Radius of circular arc HI |
| $\tau$ | normal equidistance of trochoid DE |
| $\omega$ | rotation speed |
| $\zeta$ | upper parametric limit of trochoid DE |
| $A_c$ | centre distance between two rotors |
| d | length of straight line IJ |
| $e_a$ | major radius of ellipse FG |
| $e_b$ | minor radius of ellipse FG |
| $e_x$ , $e_y$ | coordinates of center point of elipse FG |
| $f_m$ | equation of meshing |
| $h_a$ | addendum of rack |
| $h_d$ | dedendum of rack |
| k | iteration number |
| L | length of rotor screw part |
| m | number of design variables |
| p | distance from point $C_1$ to $y_h$-axis (Fig. 3) |
| $r_d$ | inner radius rotor |
| $r_o$ | outer radius rotor |
| $r_p$ | pitch radius rotor |
| $\mathbf{r}_i$ $(x_i, y_i, z_i)$ | position vector in coordinate system $S_i$ |
| $S_i$ | coordinate system $i$ |
| s | length of straight line GH |
| t | length of straight line BC |
| u | pressure angle in high-pressure side of the rack |

| | |
|---|---|
| v | pressure angle in low-pressure side of the rack |
| $\mathbf{V}_i$ | sliding velocity in coordinate system $S_i$ |
| W | transverse circular pitch of rack |
| z | tooth number of rotor |
| **Subscrips** | |
| 1 | Male rotor |
| 2 | Female rotor |

## Bibliography


[1] N. Stosic, I.K. Smith, A. Kovacevic, E. Mujic, Geometry of Screw Compressor Rorors and their Tools, *Journal of Zhejiang University*, *12*, 310-326 (2011)
[2] H. Kazunori, Water-Flooded Oil- Free Screw Compressor GP series, *IHI Engineering review*, *41*, 4 (2008)
[3] A. Kovacevic, Boundary Adaptation in Grid Generation for CFD Analysis of Screw Compressor, *International Journal for Numerical Methods in Engineering*, *64*, 401-426 (2005)
[4] N. Stosic, I. Smith, A. Kovacevic, Screw Compressor - Mathematical Modeling and Performance Calculation, Berlin (2005)
[5] R. Abgrall, H. Beaugendre, C. Dobrzynki, An immersed boundary method using unstructured anisotropic mesh adaptation combined with level-sets andpenalization techniques, *Journal of Computational Physics* , *257*, 83-101 (2014)
[6] A. Ferrero, Computational fluid dynamics for aerospace propulsion systems: an approach based on discontinuous finite elements, 155 (2015)
[7] J.A. Sethian, Level Set Methods and Fast Marching Methods: Evolving Interfaces in Computational Geometry, London (1996)
[8] V. Dolejsi, M. Feistauer, Discontinuous Galerkin Method - Analysis and Applications to Compressible Flow, Switzerland (2015)
[9] S. Gottlieb, C-W. Shu, Total variation diminishing Runge-Kutta schemes, *Math. Comput.* , *67*, 73-85 (1998)
[10] https://en.wikipedia.org/wiki/Roots-type_supercharger
[11] A. Rohatgi , WebPlotDigitizer
[12] Worldwide.espacenet.com. 1939-10-03. Retrived 2014-07-22
[13] Sakun I.A. , Vintovie kompresorii (Screw Compressors), Mashinostroenie, Leningrad (1960)
[14] Andreev P.A. , Vintovie kompressornie mashinii (Screw CompressionMachines), SUDPROM Leninngrad (1961)
[15] Amosov P.E., intovie kompresornie mashinii – Spravochnik(Screw Compression Machines-Handbook), Mashinstroienie, Leningrad (1977)
[16] Rinder L., Schraubenverdichter (Screw Compressors), New York (1979)
[17] Konka K-H, Schraubenkompressoren (ScrewCompressors), Duesseldorf (1988)

[18] O'Neil P.A., Industrial Compressors, Theory and Equipment, Oxford (1993)
[19] Arborn I.M., The Design and Application of Rotary Twin-shaft Compressors in the Oil and Gas Process Industry, London (1994)
[20] Xing Z.W. , Screw Compressors: Theory, Design and Application, Beijing, China (2000)
[21] Nilson, US Patent 2, 622, 787 (1952)
[22] Shibbie, US Patent 4,140,445 (1979)
[23] Astberg A., Patent GB 2092676B (1982)
[24] Ohman H. , PCT Patent WO 98/27340 (1999)
[25] N. Stosic, K, Hanjalic, Development and Optimization of Screw Machines With a Simulation Model - Part I: Profile Generation, *Journal of Fluids Engineering*, *119*, 659-663 (1997)
[26] Y. Wu, Z. Fong, Optimization design of an explicitly defined racj for the generation of rotors for twin-screw compressors, *Mechanism and Machine theory* , *44*, 66-82 (2008)
[27] N. Stosic, U.S. Patent No. 6,296,461 B1 (2001)
[28] Y. Wu, Z. Fong, Rotor Profile Design For the Twin-Screw Compressor Based on the Normal-Rack Generation Method, *Journal of Mechanic Design*, *130*, 8 (2008)
[29] F.L. Litvin, Litvin, Teoria zubchanih zaceplenii (Theory of Gearing), Moscow (1956)
[30] Y. Wu, Z. Fong, Improved rotor profiling based on the arbitrary sealing line for twin-screw compressors, *Mechanism and Machine Teory*, *43*, 695-711 (2008)
[31] A. Ferrero, F. Larocca, G. Puppo, A robust and adaptative recovery-based discontinuous Galerkin method for the numerical solution of convection-diffusion equations, *Internationa Journal for Numeric Methods in Fluids*, *77*, 63-91 (2015)
[32] D. Canuto, K. Taira, Two-dimensional compressible viscous flow around a circular cylinder, *Journal of Fluid Mechanics*, *785*, 349-371 (2015)
[33] Norberg C., Fluctuating lift on a circular cylinder: reviw and new measurements, *Journal of Fluids and Structures*, *6*, 547-567 (2003)
[34] Tritton DJ, Experiments on the flow past a circular cylinder at low Reynolds number, *Journal of Fluid Mechanics*, *6*, 547-567 (1959)
[35] von Wieselsberger C., Neuere festellungen aber die gesetze des flassigkeits un luftwiderstands , *Phys. Z.*, *22*, 321-328 (1921)

[36] Williamson CHK, Oblique and parallel modes of vortex shedding in the wake of a circular cylinder at low Reynolds number, *Journal of Fluid Mechanics*, *206*, 579-627 (1989)
[37] M. Bar-Lev, H.T. Yang, Initial flow field over an impulsively started cylinder, *Journal of Fluid Mechanic*, *72*, 625-647 (1975)
[38] P. Koumoutsakos, A. Leonard, High-resolution simulations of the flow around an impulsively started cylinder using vortex method, *Journal of Fluid Mechanic*, *296*, 1-38 (1995)
[39] D. Guerrato, J.M. Nouri, N. Stosic and C. Arcoumanis, Flow and pressure characteristics within a screw compressor, *Journal of Physics: Conference Series*, *85*, 012-012 (2007)
[40] S. Rane, A. Kovacevic, N. Stosic, M. Kethidi, Grid deformation strategies for CfD analysis of screw compressor, *Internationa journal of refrigeration*, *36*, 1883-1893 (2013)
[41] Q. Liu, O.V. Vasilyev, A Brinkman penalizatin method for compressible flows in complex geometries, *Journal of Computatonal Physics*, *227*, 946-966 (2007)